

## Supplemental Material for High-pressure Synthesis of Rubidium Superhydrides

Mikhail A. Kuzovnikov, Busheng Wang, Xiaoyu Wang, Tomas Marqueno,  
Hannah A. Shuttleworth, Calum Strain, Eugene Gregoryanz,  
Eva Zurek, Miriam Pena-Alvarez, and Ross T. Howie

### Experimental Details

We used symmetric Mao-type DACs with wide apertures and ultra-low fluorescence Boehler-Almax diamonds. For pressures below 60 GPa we used diamonds with flat culets with a diameter of 200  $\mu\text{m}$  (runs 6, 7, 8, 9, 11, 13, 14, 17, 18) or 300  $\mu\text{m}$  (run 12). For higher pressures, we used diamonds with culets of 100 (runs 10, 15, 19, 20, 21) or 70  $\mu\text{m}$  (run 16) bevelled at  $8^\circ$  to a diameter of 300  $\mu\text{m}$ . Rhenium gaskets were used in all experimental runs with a sample chamber of initial diameter of  $\sim 60\%$  of the culet. Rubidium (99.75% purity, Alfa Aesar) was loaded into DACs in argon glovebox with residual oxygen and moisture content less than 0.1 ppm, the cell was clamped with screws and transferred to a high-pressure gas loading apparatus. The system was flushed and vented 4 times with hydrogen gas (99.9995% purity, BOC); after reaching a gas pressure of 0.2 GPa, the DAC was opened and clamped again with screws, and extracted from the gas-loading apparatus. Further compression was realized with either screws or a gas membrane. Hydrogen was always in excess unless otherwise stated, serving both as a reagent and as the pressure-transmitting medium.

A custom-built backscattering micro-Raman setup was used to collect Raman spectra. We used a 514.53 nm Ar-laser (Innova 70C, Coherent), with the typical output power of 20 mW as the excitation source. An Acton SP-2500i spectrometer (Princeton Instruments) equipped with a 300  $\text{mm}^{-1}$  grating and a liquid nitrogen cooled PyLoN CCD (Princeton Instruments) was used. Before collecting each spectrum, the spectrometer was calibrated using the Ar + Ne lamp. The resolution and the spectral accuracy was about 3  $\text{cm}^{-1}$ .

Angular-dispersive powder X-ray diffraction experiments were performed at the Extreme Conditions Beamline (ECB, P02.2) at PETRA-III, Hamburg, Germany [liermann2015], at the ID15-b [merlini2013] and ID27 beamlines at the ESRF, Grenoble, France, at the 13-IDD beamline at Advances Photon Source, Argonne, USA [prakapenka2008], and at the I15 beamline at Diamond Light Source, Didcot, UK [anzellini2018]. Typically, the cell was oscillated around  $\omega$  axis by  $\pm 15^\circ$ , and the 2D diffraction image was collected for 20-30 s.

At P02.2, we used an incident X-ray beam with  $E = 42.4$  keV ( $\lambda \approx 0.292$  Å), focused to a  $\sim 2 \times 2$   $\mu\text{m}^2$  spot using Kirkpatrick-Baez mirrors. Diffraction images were recorded using Perkin Elmer XRD1621 detector with a sample-to-detector distance (SDD) of  $\sim 400$  (run 21) or  $\sim 424$  mm (runs 18, 19), as calibrated with a CeO<sub>2</sub> standard.

At ID15-b an incident beam with  $E \approx 30.2$  keV ( $\lambda \approx 0.410$  Å) was focused to about 20  $\mu\text{m}$  (runs 1, 6) or  $\sim 1$   $\mu\text{m}$  spot (run 20). The diffraction patterns were collected with MAR345 detector with SDD  $\approx 280$  mm (run 1), or with EIGER2 X 9M detector with SDD  $\approx 250$  (run 6) or 181 mm (run 20). In each case the SDD was calibrated using a Si powder standard.

At ID27 an incident beam with  $E \approx 46.8$  keV ( $\lambda \approx 0.265$  Å) was focused to a  $\sim 2 \times 4$   $\mu\text{m}^2$  spot, and EIGER2 X 9M CdTe detector was used for data collection (runs 9, 10, 11, 12). The SDD  $\approx 361$  mm was calibrated with a CeO<sub>2</sub> standard.

At 13IDD an incident beam with  $E \approx 42.0$  keV ( $\lambda \approx 0.2952$  Å) was focused onto a  $\sim 2 \times 2$   $\mu\text{m}^2$  spot, and Pilatus3X 1M detector was used for data acquisition. The SDD  $\approx 207$  mm was calibrated with a LaB<sub>6</sub> standard.

At I15 an incident beam with  $E \approx 29.2$  keV ( $\lambda \approx 0.425$  Å) was collimated down to  $\sim 20$   $\mu\text{m}$ . We used MAR345 detector with SDD  $\approx 501$  mm, calibrated with a CeO<sub>2</sub> standard, to record the diffraction patterns in run 2, and Pilatus3 2M detector with SDD  $\approx 403$  mm, calibrated with a LaB<sub>6</sub> standard, was used to record the diffraction in run 8.

The SDD, detector orientation and wavelength calibration, primary processing, azimuthal integration and background subtraction were done with the DIOPTAS v0.5.5 software [prescher2015]. Phase analysis and Rietveld refinements were done with the POWDERCELL 2.4 program [kraus1996].

Pressure was determined with one of the following four methods. In several cells (runs 6, 9, 12, 10, 19, 20, and 21) we had an internal gold standard for pressure determination by X-ray diffraction using the previously established  $V(P)$  equation of state of gold [dorfman2012]. With this pressure scale, we constructed the  $V(P)$  equation of state for RbH-II, which parameters are indicated in Table SMII. This equation of state is in a good agreement with previous data [ghandehari1995] for RbH compression without pressure transmitting medium. For the rest of the cells, which did not have internal gold standard, the pressure in XRD experiments was determined with our RbH-II equation of state.

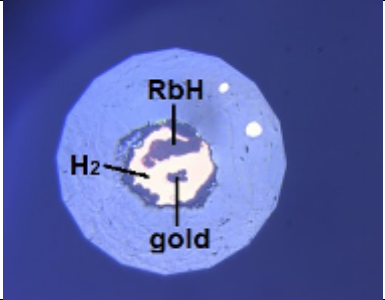
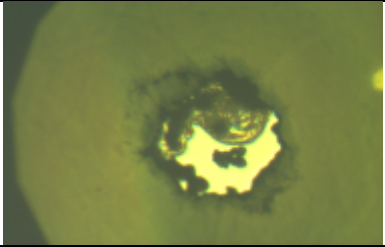
In most of the Raman experiments, the pressure was determined from the frequency of free H<sub>2</sub> vibron, determined previously [howie2012]. The dependence of the H<sub>2</sub> vibron frequency on pressure has a maximum at 34 GPa, which results in a large uncertainty of pressure determination with H<sub>2</sub> vibron scale in its vicinity. Thus, between 25 and 45 GPa we additionally corrected the pressure value using the diamond Raman edge scale [akahama2006]. It should be noted that the diamond Raman edge scale alone [akahama2006] typically overestimates the pressure by  $\sim 5$ -10%. The accuracy of pressure determination below 25 GPa was about 0.5 GPa, and above that it was about 2 GPa. In run 14 we used ruby fluorescence method with quasi-hydrostatic pressure scale [mao1986], which provided an accuracy of 0.3 GPa.

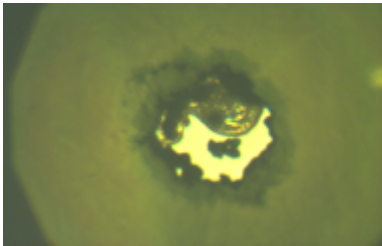
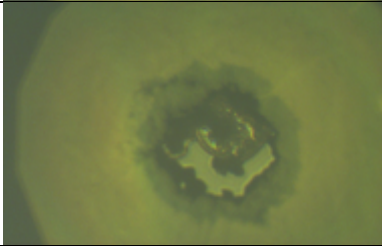
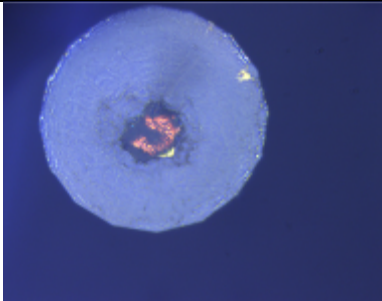
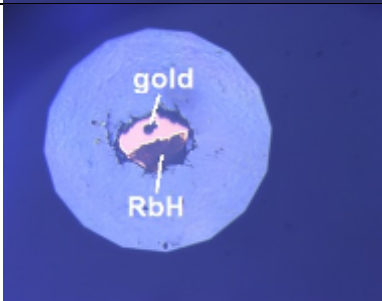
Laser heating in home-based optical experiments was realized with a custom-built optical setup, which employed a continuous-wave 1070 nm Yb-doped fiber laser (YLR-200-AC, IPG Photonics). Because rubidium hydrides are transparent (except for RbH<sub>5</sub>-II, which has an orange tint at 100 GPa), the IR radiation did not couple well with the samples. We gradually increased the output power from 10 to about 40 W and moved the sample with respect to the laser beam to produce short flashes in various spots on the sample. The temperature in the flashes could be estimated to be of the order of 1000-2000 K. Laser heating in XRD experiments were done with the laser heating setup at the respective XRD beamlines.

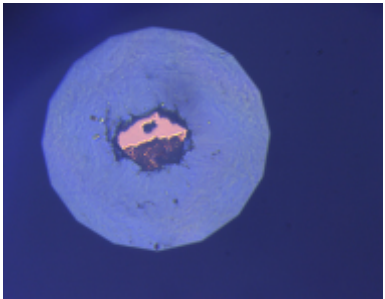
**Table SMI.** List of samples synthesized and studied in this work. The pressures indicated below were determined with H<sub>2</sub> vibron frequency scale [howie2012] and with ruby fluorescence method [mao1986] (run 14) for Raman experiments, and with gold [dorfman2012] or RbH-II (present work, Table SMII) equations of state for X-ray diffraction experiments. The indicated pressures of laser heating were measured after it.

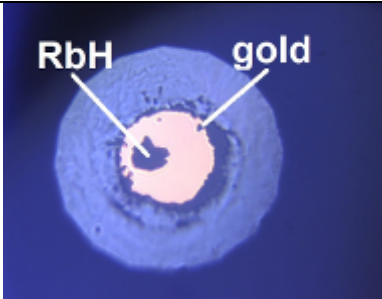
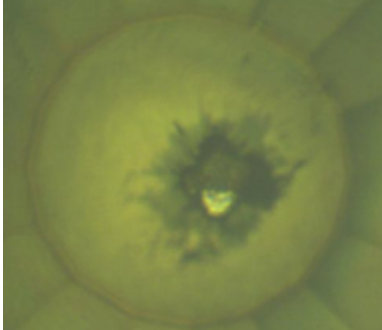
No.	Photo (reflection+transmission)	Synthesis conditions	Raman features, cm <sup>-1</sup>	Phase analysis results
1	n/a	Rb+H <sub>2</sub> compressed to 37 GPa and laser heated	n/a	After heating: RbH-II with a=2.903 Å+RbH <sub>9</sub> -II with a=4.175 Å c=3.344 Å
	n/a	Decompressed to 15 GPa	n/a	RbH-II with a=3.156 Å+minor RbH <sub>9</sub> -II with a=4.579 Å c=3.749 Å+minor impurity. The pattern at 22 GPa is shown in Fig. 1b
2	n/a	Rb+H <sub>2</sub> compressed to 4.7 GPa	n/a	RbH-II with a=3.340 Å+RbOH-II(Cmcm) with a=3.945 Å b=10.441 Å c=4.056 Å
	n/a	Compressed to 32 GPa	n/a	RbH-II with a=2.946 Å
	n/a	Laser heated at 33 GPa	n/a	RbH-II with a=2.937 Å+minor RbH <sub>9</sub> -II with a=4.199 Å c=3.420 Å+minor impurity
3	n/a	Rb+H <sub>2</sub> compressed to 34 GPa and laser heated	Free H <sub>2</sub> vibron at 4268; split bound H <sub>2</sub> vibron at 3863-3932, peaks at 367, 463, 508, 701, and 783 (likely, RbH <sub>9</sub> -II)	n/a
	n/a	Decompressed to 14.1 GPa	RbH <sub>9</sub> -II converted into RbH <sub>9</sub> -I. Free H <sub>2</sub> vibron at 4244; bound H <sub>2</sub> vibron at 3835	n/a

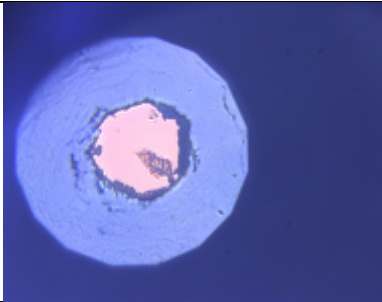
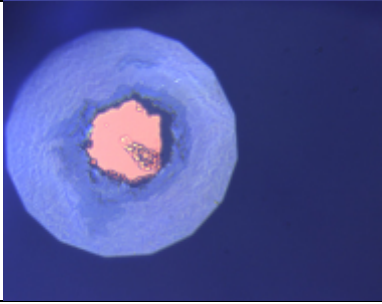
			with satellite at 4046, peaks at 336, 731, 785, and 891	
	n/a	Compressed to 19.7 GPa	Free H <sub>2</sub> vibron at 4257; bound H <sub>2</sub> vibron at 3838 with satellite at 4073, peaks at 360, 455, and 786 (likely, RbH <sub>9</sub> -I)	n/a
	n/a	Decompressed to 7.2 GPa	Free H <sub>2</sub> vibron at 4215+free H <sub>2</sub> rotons. RbH <sub>9</sub> -I decomposed into RbH-II	n/a
4	n/a	Rb+H <sub>2</sub> compressed to 19.4 GPa and laser heated	Free H <sub>2</sub> vibron at 4256; bound H <sub>2</sub> vibron at 3828 with satellite at 4061, peaks at 353 and 757 (likely, RbH <sub>9</sub> -I)	n/a
	n/a	Compressed to 38 GPa	Free H <sub>2</sub> vibron at 4267; bound H <sub>2</sub> vibron at 3841 with satellite at 4140, peaks at 386 and 866 (likely, RbH <sub>9</sub> -I)	n/a
	n/a	Compressed to 47 GPa	RbH <sub>9</sub> -I converted into RbH <sub>9</sub> -II. Free H <sub>2</sub> vibron at 4259; broad bound H <sub>2</sub> vibron at 3936, peaks at 399 and 734 (likely, RbH <sub>9</sub> -II)	n/a
	n/a	Decompressed to 34 GPa	Free H <sub>2</sub> vibron at 4268; split bound H <sub>2</sub> vibron at 3885-3933, peaks at 389 and 712 (likely, RbH <sub>9</sub> -II)	n/a
5	n/a	Rb+H <sub>2</sub> compressed to 20.4 GPa and laser heated	Free H <sub>2</sub> vibron at 4258; bound H <sub>2</sub> vibron at 3832 with satellite at 4070, peaks at 358 and 779 (likely, RbH <sub>9</sub> -I)	n/a
	n/a	Compressed to 41 GPa	Free H <sub>2</sub> vibron at 4265; bound H <sub>2</sub> vibron at 3860 with satellite at 4151, peaks at 393 and 872 (likely, RbH <sub>9</sub> -I)	n/a

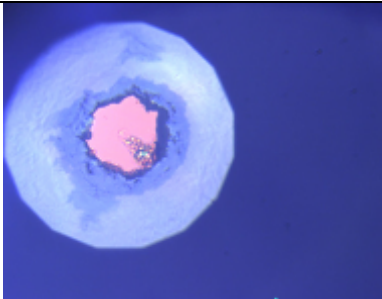
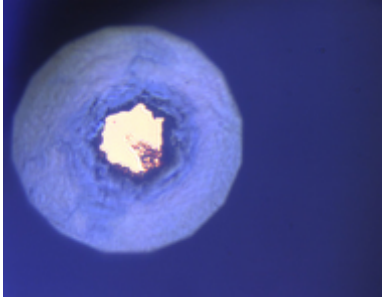
	n/a	Decompressed to 13.4 GPa	Free H <sub>2</sub> vibron at 4242; bound H <sub>2</sub> vibron at 3832 with satellite at 4038, peaks at 336 and 709 (likely, RbH <sub>9</sub> -I)	n/a
6		Rb+H <sub>2</sub> compressed to 2.0 GPa	Free H <sub>2</sub> vibron at 4181, free H <sub>2</sub> rotons; trace peak at 3416 (RbOH)	At 3.7 GPa: RbH-II with a=3.387 Å+traces of RbOH-II(Cmcm) with a=3.988 Å b=10.557 Å c=4.09 Å+Au with a= 4.051Å
	n/a	Compressed to 13 GPa and laser heated	n/a	After heating at 15 GPa: RbH-II with a=2.981 Å+Au with a=3.981 Å+trace impurity
		Compressed to 26 GPa	n/a	RbH-II with a=3.116 Å+Au with a=3.929 Å+trace impurity
	n/a	Laser heated at 29 GPa	Free H <sub>2</sub> vibron at 4264; bimodal bound H <sub>2</sub> vibron at 3848-3927 (RbH <sub>9</sub> -II); bound H <sub>2</sub> vibron at 4109, peak at 2260 (diamond-like phase)	Diamond-like phase with a=9.066 Å+RbH <sub>9</sub> -II with a=4.18 Å c=3.53 Å+Au with a=3.917 Å+minor impurity

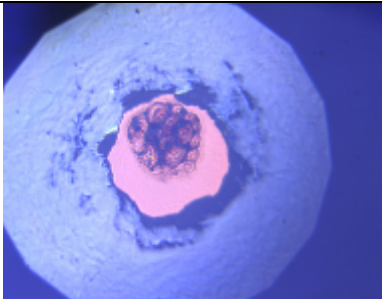
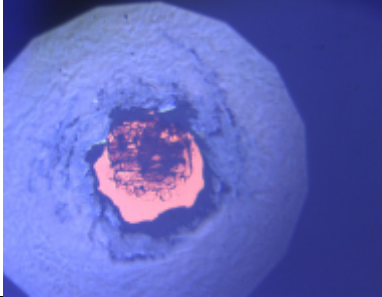
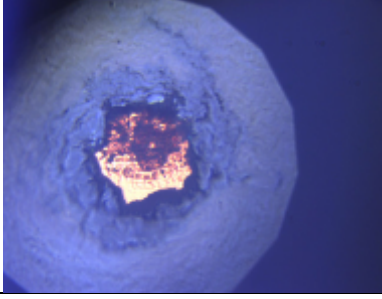
		Compressed to 42 GPa	Free H <sub>2</sub> vibron at 4264; broad bound H <sub>2</sub> vibron at 3920 (RbH <sub>9</sub> -II); bound H <sub>2</sub> vibron at 4108 with a satellite at 4141, bimodal peak at 2290-2330 (diamond-like phase)	RbH <sub>9</sub> -II with a=4.091 Å c=3.358 Å+Au with a=3.869 Å+traces of diamond-like phase with a=8.79 Å +minor impurity
		Laser heated at 46 GPa	Free H <sub>2</sub> vibron at 4262; bound H <sub>2</sub> vibron at 4106 with a satellite at 4143, bimodal peak at 2303-2351, peaks at 481, 931 and 1161 (diamond-like phase)	Diamond-like phase with a=8.652 Å+minor impurity (see Fig. SM6)
		Decompressed to 9GPa	Free H <sub>2</sub> vibron at 4223, free H <sub>2</sub> rotons, broad peak at 2075 (impurity)	Diamond-like phase decomposed between 13.5-8.8 GPa. RbH-II with a=3.209 Å+Au with a=4.017 Å+impurity
7		Rb+H <sub>2</sub> compressed to 16.3 GPa	Free H <sub>2</sub> vibron at 4250, free H <sub>2</sub> rotons	n/a

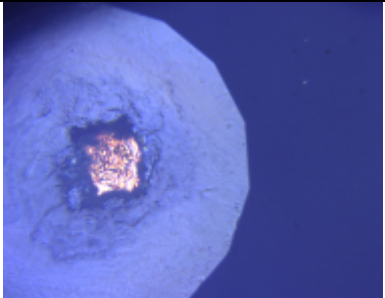
		Laser heated at 17.6 GPa	Free H <sub>2</sub> vibron at 4253, free H <sub>2</sub> rotors; bound H <sub>2</sub> vibron at 3832 with a satellite at 4061 (likely, RbH <sub>9</sub> -I)	n/a
8	n/a	Rb+H <sub>2</sub> compressed to 38 GPa and laser heated	n/a	RbH <sub>9</sub> -II with a=4.157 Å c=3.297 Å+RbH-II with a=2.893 Å+RbH <sub>5</sub> -I with a=3.366 Å b=8.029 Å c=5.355 Å
	n/a	Compressed to 42 GPa	n/a	RbH <sub>9</sub> -II with a=4.109 Å c=3.296 Å+RbH-II with a=2.875 Å+traces of RbH <sub>5</sub> -I
		Decompressed to 33 GPa	At 37 GPa, free H <sub>2</sub> vibron at 4267; bimodal bound H <sub>2</sub> vibron at 3858-3919, peaks at 129, 388, 501, 707, 807, 983 (RbH <sub>9</sub> -II). See orange curve in Fig. 3a.	RbH-II with a=2.933 Å+RbH <sub>9</sub> -II with a=4.234 Å c=3.420 Å+RbH <sub>5</sub> -I with a=3.430 Å b=8.165 Å c=5.412 Å
	n/a	Decompressed to 22 GPa	n/a	RbH-II with a=3.032 Å+RbH <sub>9</sub> -II with a=4.381 Å c=3.596 Å+RbH <sub>5</sub> -I with a=3.570 Å b=8.435 Å c=5.610 Å
9	At 3.0 GPa:	Rb+H <sub>2</sub> compressed to 20 GPa	At 3.0 GPa: free H <sub>2</sub> vibron at 4193, free H <sub>2</sub> rotors; trace peak at 3416 (RbOH)	At 20 GPa: RbH-II with a=3.050 Å+Au with a=3.954 Å

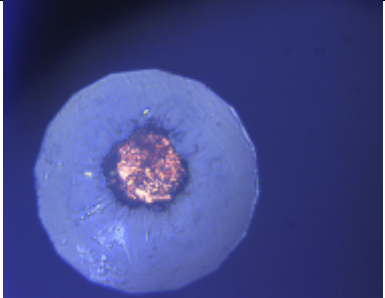
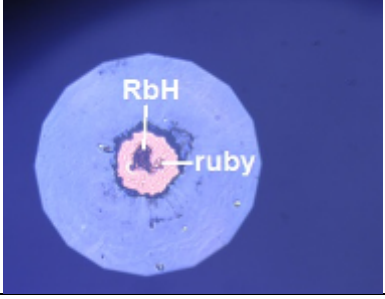
				
10		Rb+H <sub>2</sub> compressed to 94 GPa	At 15.7 GPa: free H <sub>2</sub> vibron at 4249, free H <sub>2</sub> rotors; trace peak at 3333 (RbOH)	At 94 GPa: RbH-II with a=2.654 Å+Au with a=3.734 Å
		Laser heated at 103 GPa	Free H <sub>2</sub> vibron at 4167; bound H <sub>2</sub> vibron at 3654, peaks at 342, 720, 901, 1032, 1081, 1151, 1260 (RbH <sub>5</sub> -II).	RbH <sub>5</sub> -II with a=5.409 Å b=4.892 Å c=3.987 Å+Au with a=3.716 Å (see Fig. 1d)
	n/a	Decompressed to 21 GPa	n/a	Between 35-21 GPa RbH <sub>5</sub> -II transformed into RbH <sub>5</sub> -I, which then partially disproportionated into RbH-II and RbH <sub>9</sub> -II. At 21 GPa: RbH-II with

				a=3.053 Å+RbH <sub>9</sub> -II with a=4.398 Å c=3.590 Å+Au with a=3.95 Å+traces of RbH <sub>5</sub> -I
	n/a	Decompressed to 7.6 GPa	n/a	RbH <sub>9</sub> -II decomposed into RbH-II between 21 and 7.6 GPa. At 7.6 GPa: RbH-II with a=3.273 Å+Au with a=4.024 Å
11		Rb+H <sub>2</sub> compressed to 8.0 GPa	Free H <sub>2</sub> vibron at 4219, free H <sub>2</sub> rotons	n/a
		Compressed to 16.7 GPa and laser heated	After heating: free H <sub>2</sub> vibron at 4251, free H <sub>2</sub> rotons	n/a

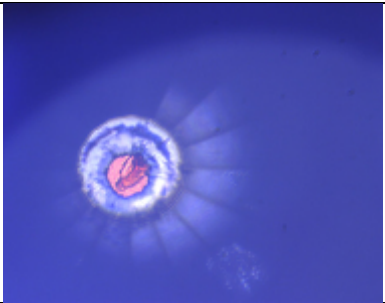
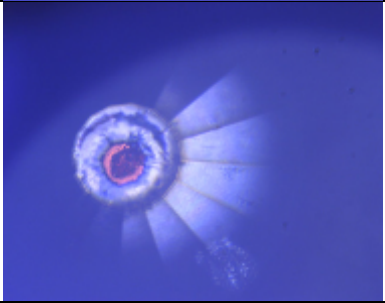
		Compressed to 22 GPa and laser heated. Compressed to 25 GPa.	At 25.5 GPa: free H <sub>2</sub> vibron at 4264, free H <sub>2</sub> rotons; bound H <sub>2</sub> vibron at 3827 with a satellite at 4080 (probably RbH <sub>9</sub> -I); impurity band at 2235	n/a
		Decompressed to 22.7 GPa	Free H <sub>2</sub> vibron at 4161, free H <sub>2</sub> rotons; bound H <sub>2</sub> vibron at 3834 with a satellite at 4078 (probably RbH <sub>9</sub> -I)	At 22.2 GPa: traces of RbH-II with a=3.03 Å+traces of RbH <sub>9</sub> -II with a=4.36 Å c=3.56 Å
	n/a	Decompressed to 8.6 GPa	RbH <sub>9</sub> -I decomposed between 8.9-8.6 GPa. At 8.6 GPa: free H <sub>2</sub> vibron at 4222, free H <sub>2</sub> rotons; impurity bands at 1046, 2108 and 4077	n/a
12		Rb+H <sub>2</sub> compressed to 16.3 GPa	Free H <sub>2</sub> vibron at 4250, free H <sub>2</sub> rotons	n/a

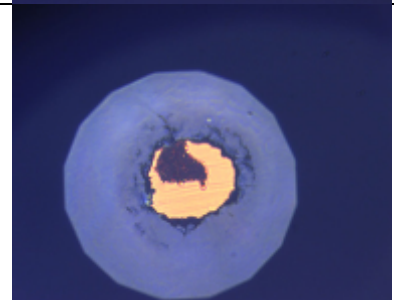
	Laser heated at 16.5 GPa	Free H <sub>2</sub> vibron at 4250, free H <sub>2</sub> rotors; impurity bands at 1605, 1470, 1830	n/a
	Compressed to 21.3 GPa and laser heated	Free H <sub>2</sub> vibron at 4259, free H <sub>2</sub> rotors; bound H <sub>2</sub> vibron at 3826 with a satellite at 4075 (RbH <sub>9</sub> -I); impurity bands at 1790, 2210	n/a
	Decompressed to 15.0 GPa	Free H <sub>2</sub> vibron at 4246, free H <sub>2</sub> rotors; bound H <sub>2</sub> vibron at 3824 with a satellite at 4058 (RbH <sub>9</sub> -I); impurity bands at 1785, 2135	RbH <sub>9</sub> -I with a=4.569 Å b=7.775 Å c=7.426 Å+RbH-II with a=3.127 Å+impurities
n/a	Compressed to 24 GPa and laser heated	n/a	RbH <sub>9</sub> -I converted into RbH <sub>9</sub> -II and diamond-like phase. RbH <sub>9</sub> -II with a=4.301 Å c=3.574 Å+diamond-like phase with a=9.201 Å+Au with a=3.935 Å

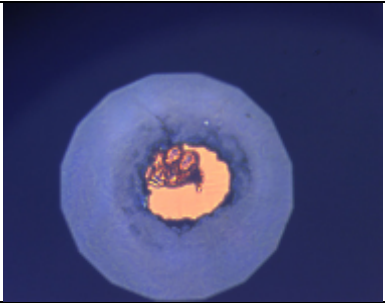
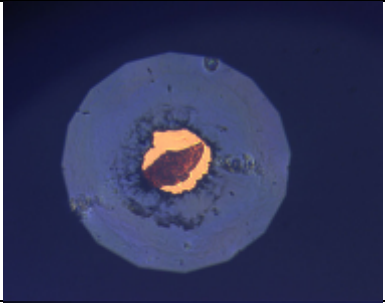
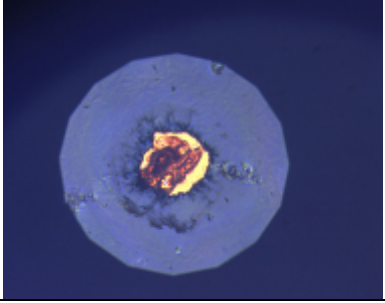
	n/a	Decompressed to 9.3 GPa	n/a	RbH <sub>9</sub> -II and diamond-like phase transformed into RbH <sub>9</sub> -I between 15-9.3 GPa. At 9.3 GPa: Au with 4.013 Å+RbH-II with a=3.219 Å+RbH <sub>9</sub> -I with a=4.70 Å b=8.01 Å c=7.66 Å
		Decompressed to 6.2 GPa	At 6.2 GPa: free H <sub>2</sub> vibron at 4209, free H <sub>2</sub> rotors; impurity band at 1820	RbH <sub>9</sub> -I decomposed into RbH-II between 9.0-7.4 GPa. At 7.4 GPa: RbH-II with a=3.27 Å+Au with a=4.025 Å
13	At 2.4 GPa: 	Rb+H <sub>2</sub> compressed to 20.7 GPa	Free H <sub>2</sub> vibron at 4259, free H <sub>2</sub> rotors; trace peak at 3282 (RbOH)	n/a

		Laser heated at 25.5 GPa	Free H <sub>2</sub> vibron at 4264, free H <sub>2</sub> rotons; satellite peak at 4281 ((CH <sub>4</sub> ) <sub>3</sub> (H <sub>2</sub> ) <sub>25</sub> ); split bound H <sub>2</sub> vibron at 3836-3910 (RbH <sub>9</sub> -II); sharp peak at 3095 ((CH <sub>4</sub> ) <sub>3</sub> (H <sub>2</sub> ) <sub>25</sub> ); peak at 376 (RbH <sub>9</sub> -II)	n/a
	n/a	Decompressed to 14.3 GPa	RbH <sub>9</sub> -II transformed into RbH <sub>9</sub> -I at 14.3 GPa. Free H <sub>2</sub> vibron at 4243, free H <sub>2</sub> rotons; bound H <sub>2</sub> vibron at 3834 with a satellite at 4047 (RbH <sub>9</sub> -I); sharp peak at 3033 ((CH <sub>4</sub> ) <sub>x</sub> (H <sub>2</sub> ) <sub>y</sub> )	n/a
		Decompressed to 8.3 GPa	RbH <sub>9</sub> -I decomposed into RbH-II at 8.3 GPa. Free H <sub>2</sub> vibron at 4222, free H <sub>2</sub> rotons; sharp peak at 3000 ((CH <sub>4</sub> ) <sub>x</sub> (H <sub>2</sub> ) <sub>y</sub> )	n/a
14		Rb+H <sub>2</sub> compressed to 19.7 GPa	Free H <sub>2</sub> vibron at 4255, free H <sub>2</sub> rotons. See black curve in Fig. SM1	n/a

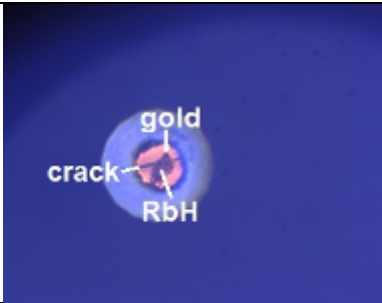
	<p>Laser heated at 22.3 GPa</p>	<p>Free H<sub>2</sub> vibron at 4257, free H<sub>2</sub> rotons; bound H<sub>2</sub> vibron at 3833 with a satellite at 4075, peaks at 96, 225, 359, 453, 789 (RbH<sub>9</sub>-I). See violet curve in Fig. SM1 and brown curve in Fig. 3a</p>	<p>n/a</p>
	<p>Compressed to 49.0 GPa</p>	<p>RbH<sub>9</sub>-I gradually converted into RbH<sub>9</sub>-II between 36.1-49.0 GPa. At 49.0 GPa: free H<sub>2</sub> vibron at 4260, free H<sub>2</sub> rotons; split bound H<sub>2</sub> vibron at 3774-3918, peaks at 122, 385, 723, 1046 (likely, RbH<sub>9</sub>-II+RbH<sub>9</sub>-I). See red curve in Fig. SM1</p>	<p>n/a</p>
	<p>Laser heated at 51 GPa</p>	<p>RbH<sub>9</sub>-II converted into a diamond-like phase. Free H<sub>2</sub> vibron at 4258; bound H<sub>2</sub> vibron at 4104 with a satellite at 4143, peak at 2373 with a satellite at 2322, peaks at 392, 498, 952, 1183 (diamond-like phase). See magenta curve in Fig. SM7</p>	<p>n/a</p>
<p>n/a</p>	<p>Decompressed to 9.5 GPa</p>	<p>Diamond-like phase decomposed into RbH<sub>9</sub>-I between 14.7-9.5 GPa. Free H<sub>2</sub> vibron at 4227, free H<sub>2</sub> rotons; bound H<sub>2</sub> vibron at 3842 with a satellite at 4025</p>	<p>n/a</p>

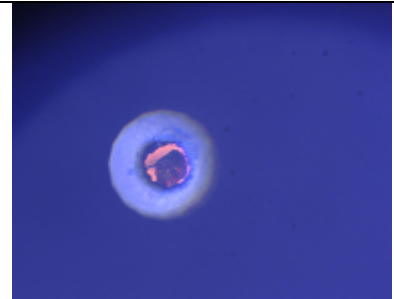
			(RbH <sub>9</sub> -I); impurity peak at 2084. See blue curve in Fig. SM7	
	n/a	Decompressed to 7.6 GPa	RbH <sub>9</sub> -I decomposed into RbH-II. Free H <sub>2</sub> vibron at 4218, free H <sub>2</sub> rotons; impurity peak at 2072. See violet curve in Fig. SM7	n/a
15		Rb+H <sub>2</sub> compressed to 99 GPa	RbH <sub>9</sub> -II started to form at 51 GPa. At 99 GPa: free H <sub>2</sub> vibron at 4173, peaks at 389, 744, 1072 (likely, RbH <sub>9</sub> -II)	n/a
		Laser heated at 101 GPa	Sample converted into RbH <sub>5</sub> -II. Free H <sub>2</sub> vibron at 4172, peaks at 147, 245, 289, 338, 736, 914, 1048, 1099, 1172, 1274 (RbH <sub>5</sub> -II)	n/a
	n/a	Decompressed to 45.4 GPa	Free H <sub>2</sub> vibron at 4245, peaks at 129, 199, 233, 277, 594, 785, 1006, 1148 (RbH <sub>5</sub> -II)	n/a

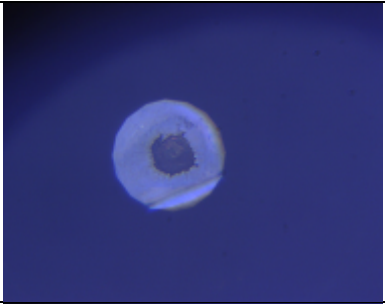
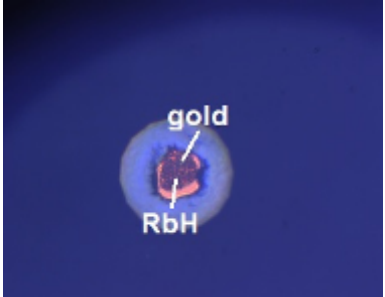
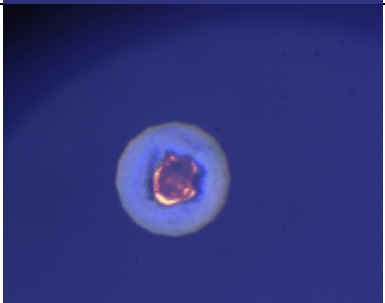
16		Rb+H <sub>2</sub> compressed to 57 GPa	RbH <sub>9</sub> -II started to form at 51 GPa. At 57 GPa: free H <sub>2</sub> vibron at 4251, free H <sub>2</sub> rotons; bound H <sub>2</sub> vibron at 3938 (likely, RbH <sub>9</sub> -II)	n/a
		Laser heated at 50 GPa	RbH <sub>9</sub> -II converted into diamond-like phase. Free H <sub>2</sub> vibron at 4259, free H <sub>2</sub> rotons; trace of bound H <sub>2</sub> vibron at 4103 (likely, diamond-like phase)	n/a
17		Rb+H <sub>2</sub> compressed to 18.7 GPa	Free H <sub>2</sub> vibron at 4255, free H <sub>2</sub> rotons	n/a

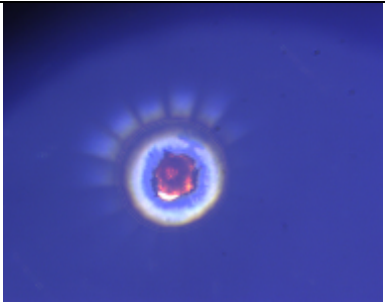
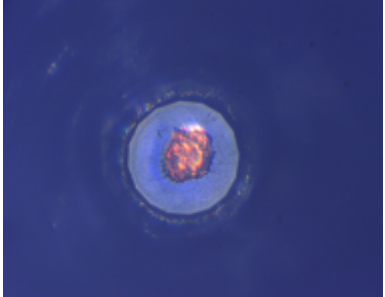
		Laser heated at 21.7 GPa	Free H <sub>2</sub> vibron at 4260, free H <sub>2</sub> rotons; split bound H <sub>2</sub> vibron at 3834-3914, peaks at 97, 357, 452, 489, 608, 687, 772 (likely, RbH <sub>9</sub> -II)	n/a
	n/a	Compressed to 47 GPa	Free H <sub>2</sub> vibron at 4262, free H <sub>2</sub> rotons; bound H <sub>2</sub> vibron at 3930, peaks at 135, 392, 542, 596, 732, 915, 1042 (likely, RbH <sub>9</sub> -II)	n/a
18		Rb+H <sub>2</sub> compressed to 16.6 GPa	Free H <sub>2</sub> vibron at 4251, free H <sub>2</sub> rotons; trace peak at 3301 (RbOH)	n/a
		Laser heated at 19.1 GPa	Free H <sub>2</sub> vibron at 4256, free H <sub>2</sub> rotons; bound H <sub>2</sub> vibron at 3828 with a satellite at 4075, peaks at 87, 352, 781 (RbH <sub>9</sub> -I)	At 23 GPa: RbH <sub>9</sub> -I with a=4.421 Å b=7.475 Å c=7.201 Å+RbH-II with a=3.028 Å+minor RbH <sub>9</sub> -II with a=4.359 Å c=3.559 Å. A pattern at 28 GPa is shown in Fig. 1a

n/a	Compressed to 54 GPa	n/a	RbH <sub>9</sub> -I with a=4.125 Å b=6.808 Å c=6.597 Å+RbH-II with a=2.811 Å+minor RbH <sub>9</sub> -II with a=4.004 Å c=3.175 Å
n/a	Laser heated at 56 GPa	n/a	RbH <sub>9</sub> -I transformed into RbH <sub>9</sub> -II and diamond-like phase. RbH-II partially transformed into RbH <sub>5</sub> -I. RbH <sub>9</sub> -II with a=3.975 Å c=3.153 Å+RbH <sub>5</sub> -I with a=3.213 Å b=7.742 Å c=5.127 Å+RbH-II with a=2.792 Å+minor diamond-like phase with a=8.457 Å
n/a	Decompressed to 14 GPa	At 12.4 GPa: free H <sub>2</sub> vibron at 4239, free H <sub>2</sub> rotons; bound H <sub>2</sub> vibron at 3834 with a satellite at 4036, peaks at 340, 738 (RbH <sub>9</sub> -I)	RbH <sub>5</sub> -I disproportionated into RbH <sub>9</sub> -II and RbH-II between 21-14 GPa. RbH <sub>9</sub> -II partially transformed into RbH <sub>9</sub> -I between 21-14 GPa. RbH <sub>9</sub> -I with a=4.58 Å b=7.82 Å c=7.47 Å+minor RbH <sub>9</sub> -II with a=4.531 Å c=3.819 Å+minor RbH-II with a=3.160 Å+minor diamond-like phase with a=9.650 Å
	Decompressed to 8.2 GPa	RbH <sub>9</sub> -I decomposed into RbH-II between 8.6-8.2 GPa. Free H <sub>2</sub> vibron at 4221, free H <sub>2</sub> rotons	n/a

19	At 7.0 GPa:	Rb+H <sub>2</sub> compressed to 54 GPa	RbH <sub>9</sub> -II started to form at 54 GPa. Free H <sub>2</sub> vibron at 4255, free H <sub>2</sub> rotons; bound H <sub>2</sub> vibron at 3928 (likely, RbH <sub>9</sub> -II)	n/a
		Laser heated at 49.2 GPa	Free H <sub>2</sub> vibron at 4260; bound H <sub>2</sub> vibron at 4262, peaks at 132, 401 (RbH <sub>9</sub> -II); bound H <sub>2</sub> vibron at 3808, peaks at 896, 1115, 155, 223, 595, 711, 775 (RbH <sub>5</sub> -I)	RbH <sub>5</sub> -I with a=3.312 Å b=7.951 Å c=5.259 Å+RbH <sub>9</sub> -II with a=4.075 Å c=3.286 Å+RbH-II with a=2.869 Å+Au with a= 3.860 Å
	n/a	Compressed to 91 GPa	n/a	RbH <sub>5</sub> -I with a=3.058 Å b=7.493 Å c=4.927 Å+RbH <sub>9</sub> -II with a=3.823 Å c=2.996 Å+RbH-II with a=2.700 Å+Au with a=3.739 Å
20		Rb+H <sub>2</sub> compressed to 46.4 GPa	RbH <sub>9</sub> -II started to form at 46.4 GPa. Free H <sub>2</sub> vibron at 4262, free H <sub>2</sub> rotons; bound H <sub>2</sub> vibron at 3903 (likely, RbH <sub>9</sub> -II)	n/a

	<p>Laser heated at 49.7 GPa</p>	<p>Free H<sub>2</sub> vibron at 4259, free H<sub>2</sub> rotors; bound H<sub>2</sub> vibron at 3925, 401, 733, 1077, 136 (RbH<sub>9</sub>-II)</p>	<p>At 47 GPa: RbH<sub>9</sub>-II with a=3.986 Å c=3.367 Å+Au with a=3.852 Å</p>
<p>n/a</p>	<p>Compressed to 92 GPa</p>	<p>n/a</p>	<p>Au with a=3.737 Å+RbH<sub>9</sub>-II with a=3.736 Å c=3.049 Å+impurity</p>
	<p>One diamond broke and pressure dropped to 33 GPa</p>	<p>Free H<sub>2</sub> vibron at 4266; bound H<sub>2</sub> vibron at 3884, peaks at 394, 718, 847, 1016, 129 (likely, RbH<sub>9</sub>-II). See brown curve in Fig. SM2</p>	<p>n/a</p>
<p>n/a</p>	<p>Decompressed to 13.7 GPa</p>	<p>RbH<sub>9</sub>-II converted into RbH<sub>9</sub>-I between 14.2-13.7 GPa. Free H<sub>2</sub> vibron at 4243, bound H<sub>2</sub> vibron at 3826 with a satellite at 4045, peaks at 348, 741, 88 (likely, RbH<sub>9</sub>-I). See cyan curve in Fig. SM2</p>	<p>n/a</p>

		Decompressed to 8.4 GPa	RbH <sub>9</sub> -I decomposed into RbH-II between 8.7-8.4 GPa. Free H <sub>2</sub> vibron at 4221, free H <sub>2</sub> rotons. See black curve in Fig. SM2	n/a
21		Rb+H <sub>2</sub> compressed to 48 GPa	RbH <sub>9</sub> -II started to form at 23.7 GPa. At 48 GPa: free H <sub>2</sub> vibron at 4161, free H <sub>2</sub> rotons; bound H <sub>2</sub> vibron at 3891 (likely, RbH <sub>9</sub> -II). See magenta curve in Fig. SM5	n/a
		Laser heated at 48 GPa	RbH <sub>9</sub> -II and RbH <sub>5</sub> -I formed from RbH-II. Free H <sub>2</sub> vibron at 4259; bound H <sub>2</sub> vibron at 3933, peaks at 395, 739, 133 (RbH <sub>9</sub> -II); bound H <sub>2</sub> vibron at 3808, peaks at 885, 1105, 148, 212, 587, 699, 763 (RbH <sub>5</sub> -I). See brown curve in Fig. SM5	At 50 GPa: RbH <sub>5</sub> -I with a=3.270 Å b=7.882 Å c=5.204 Å+RbH <sub>9</sub> -II with a=4.067 Å c=3.250 Å+RbH-II with a=2.814 Å+Au with a=3.843 Å. See Fig.1c
	n/a	Compressed to 92 GPa	n/a	RbH <sub>9</sub> -II with a=3.841 Å c=2.996 Å+RbH <sub>5</sub> -I with a=3.050 Å b=7.506 Å c=4.931 Å+Au with a=3.737 Å.

	<p>Laser heated at 87 GPa</p>	<p>At 80 GPa: free H<sub>2</sub> vibron at 4210; bound H<sub>2</sub> vibron at 3677, peaks at 148, 232, 323, 682, 868, 1029, 1107, 1226 (RbH<sub>5</sub>-II), see brown curve in Fig. SM4; bound H<sub>2</sub> vibron at 3995, peaks at 406, 756, 1027, 1210 (RbH<sub>9</sub>-II); bound H<sub>2</sub> vibron at 3789, peaks at 1042, 1266, 1587, 2152, 178, 278, 651, 849, 910 (RbH<sub>5</sub>-I), see red curve in Fig. SM5 and dark blue curve in Fig. 3a (at 79 GPa).</p>	<p>Most of RbH<sub>9</sub>-II and RbH<sub>5</sub>-I converted into RbH<sub>5</sub>-II. At 87 GPa: RbH<sub>5</sub>-II with a=5.485 Å b=4.964 Å c=4.083 Å+minor RbH<sub>9</sub>-II with a=3.847 Å c=2.997 Å+minor RbH<sub>5</sub>-I with a=3.044 Å b=7.478 Å c=4.917 Å+Au with a=3.748 Å</p>
<p>n/a</p>	<p>Decompressed to 26.3 GPa</p>	<p>Between 35.3-26.3 GPa RbH<sub>5</sub>-II converted into RbH<sub>5</sub>-I. At 26.3 GPa: free H<sub>2</sub> vibron at 4266; bound H<sub>2</sub> vibron at 3819, peaks at 799, 979, 138, 384 (likely, RbH<sub>5</sub>-I), see dark blue curve in Fig. SM4; split bound H<sub>2</sub> vibron at 3851-3910, peaks at 383, 698, 789, 979, 125 (likely, RbH<sub>9</sub>-II)</p>	<p>n/a</p>
<p>At 19 GPa:</p> 	<p>Decompressed to 11.7 GPa</p>	<p>Between 19.6-15.0 GPa RbH<sub>5</sub>-I disproportionated into RbH<sub>9</sub>-II+RbH<sub>5</sub>-II, see dark blue curve in Fig. SM5. Between 15-13 GPa RbH<sub>9</sub>-II transformed into RbH<sub>9</sub>-I, see violet curve in Fig. SM5. At 13 GPa: bound H<sub>2</sub> vibron at 3833 with a satellite at 4047, peak at 760 (probably, RbH<sub>9</sub>-I)</p>	<p>n/a</p>

	n/a	Decompressed to 9.0	RbH <sub>9</sub> -I decomposed into RbH-II at 9 GPa, see black curve in Fig. SM5. Free H <sub>2</sub> vibron at 4225; peak at 769 (impurity)	n/a
--	-----	---------------------	--	-----

**Table SMII.** Crystal structures of experimentally observed rubidium hydrides (hydrogen atom positions unknown)

Compound	RbH-II	RbH <sub>9</sub> -I	RbH <sub>9</sub> -II	RbH <sub>5</sub> -I	RbH <sub>5</sub> -II
Space Group	<i>Fm<math>\bar{3}m</math></i> (221)	<i>Cmcm</i> (63)	<i>P6/mmm</i> (191)	<i>Cmcm</i> (63)	<i>Imma</i> (74)
Lattice Parameters at 50 GPa (Å)	a=2.822	a=4.145 b=6.839 c=6.644	a=4.009 c=3.272	a=3.270 b=7.874 c=5.209	a=5.710 b=5.122 c=4.368
Atomic coordinates	Rb 1a 0 0 0	Rb 4c 0 0.33 ¼	Rb 1a 0 0 0	Rb 4c 0 0.07 ¼	Rb 4e 0 ¼ 0.12

**Table SMIII.** Fitted parameters of the Birch-Murnaghan [birch1947] equation of state  $P = \frac{3B_0}{2} \left[ \left( \frac{V}{V_0} \right)^{-7/3} - \left( \frac{V}{V_0} \right)^{-5/3} \right] \left\{ 1 + \frac{3}{4} (B'_0 - 4) \left[ \left( \frac{V}{V_0} \right)^{-3/2} - 1 \right] \right\}$  for presently studied rubidium hydrides. We assumed the pressure  $P$  to be an independent variable and numerically solved the Birch-Murnaghan equation with respect to  $V$  for all values of the fitting parameters  $V_0$  and  $B_0$  and experimental  $P$  values. The bulk modulus pressure derivatives  $B'_0$  had a fixed value of  $B'_0 = 4$ , which is typical of many metals and hydrides. The resulting fits are shown by the dashed curves in Fig. 2a.

Compound	Pressure range (GPa)	$V_0$ (Å <sup>3</sup> /Rb atom)	$B_0$ (GPa)	$B'_0$	Source
RbH-II	3.5-104	44.0(3)	16.9(2)	4.27(2)	[ghandehari1995]
RbH-II	2.8-94	44.5(20)	18.6(50)	4(fixed)	present
RbH <sub>9</sub> -I	9-52	104(7)	12.7(50)	4(fixed)	present
RbH <sub>9</sub> -II	13-101	120(20)	7.2(80)	4(fixed)	present
RbH <sub>5</sub> -I	21-92	75(10)	12(10)	4(fixed)	present
RbH <sub>5</sub> -II	35-103	49.6(20)	47(13)	4(fixed)	present
Diamond-like phase	14-59	186(20)	10.4(70)	4(fixed)	present

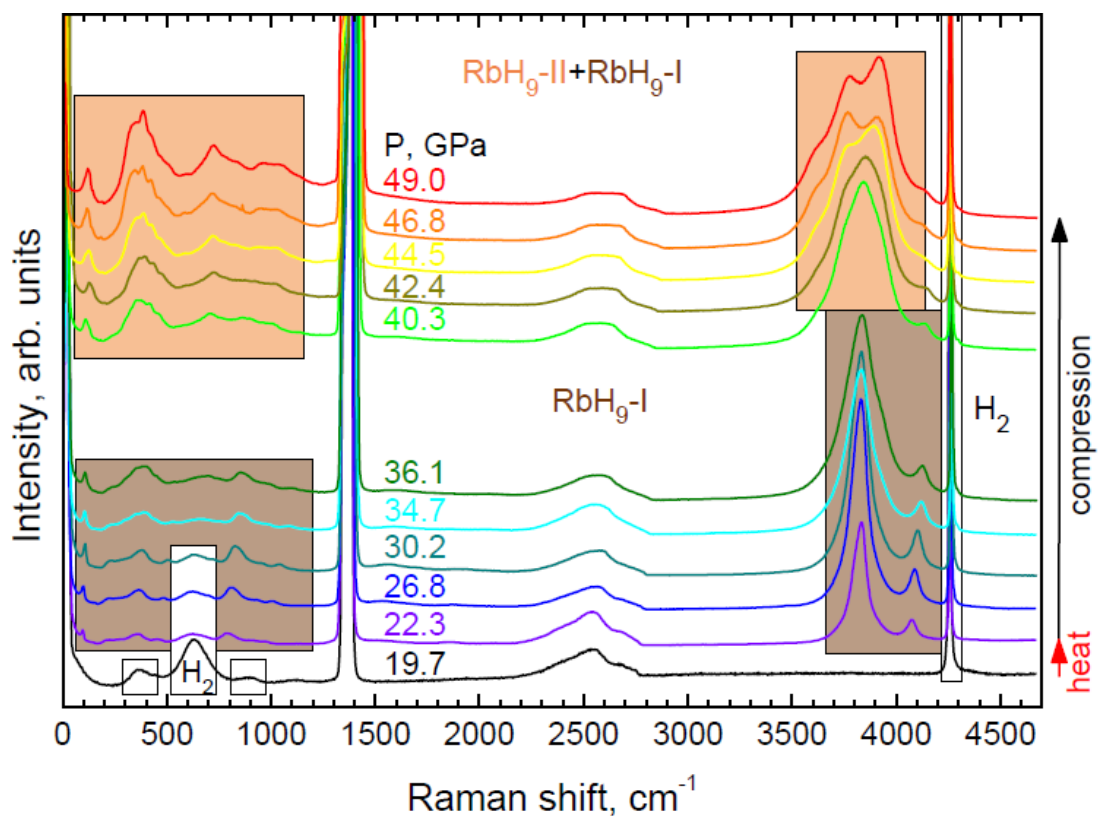


**Fig. SM1.** Characteristic Raman spectra of  $\text{RbH}_9\text{-I}$ , recorded in run 14 upon laser heating and compression at room temperature.

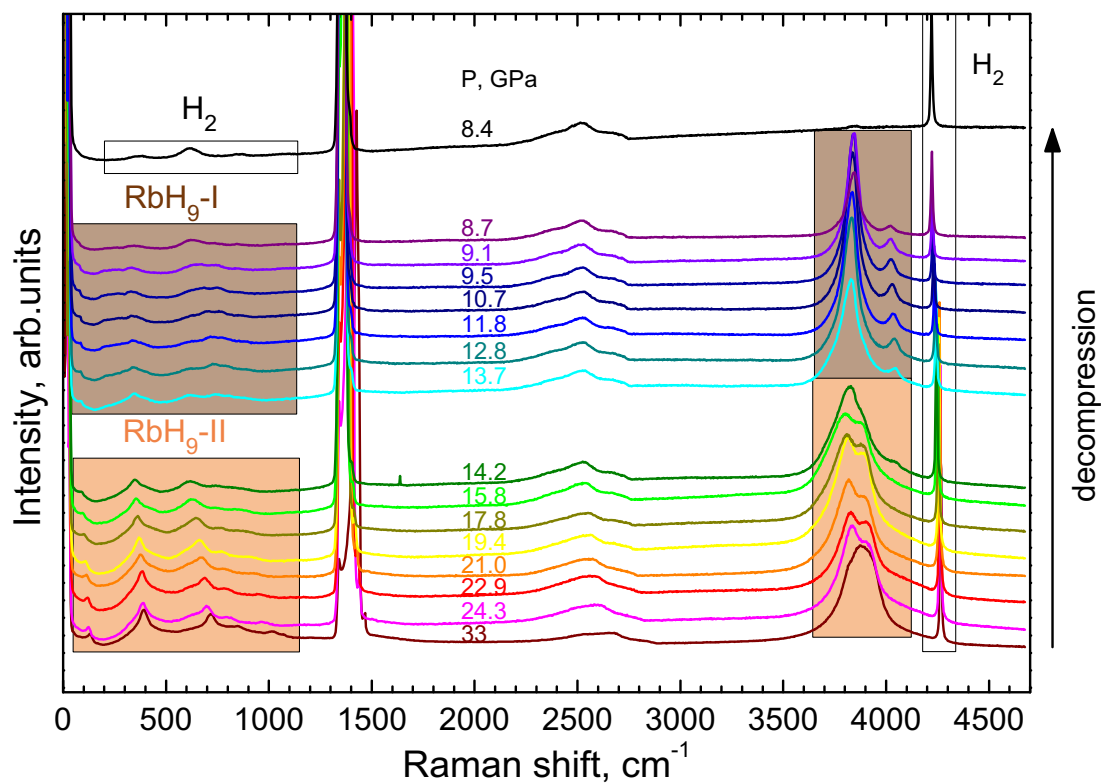


**Fig. SM2.** Characteristic Raman spectra of  $\text{RbH}_9\text{-II}$ , recorded in run 20 upon decompression at room temperature.

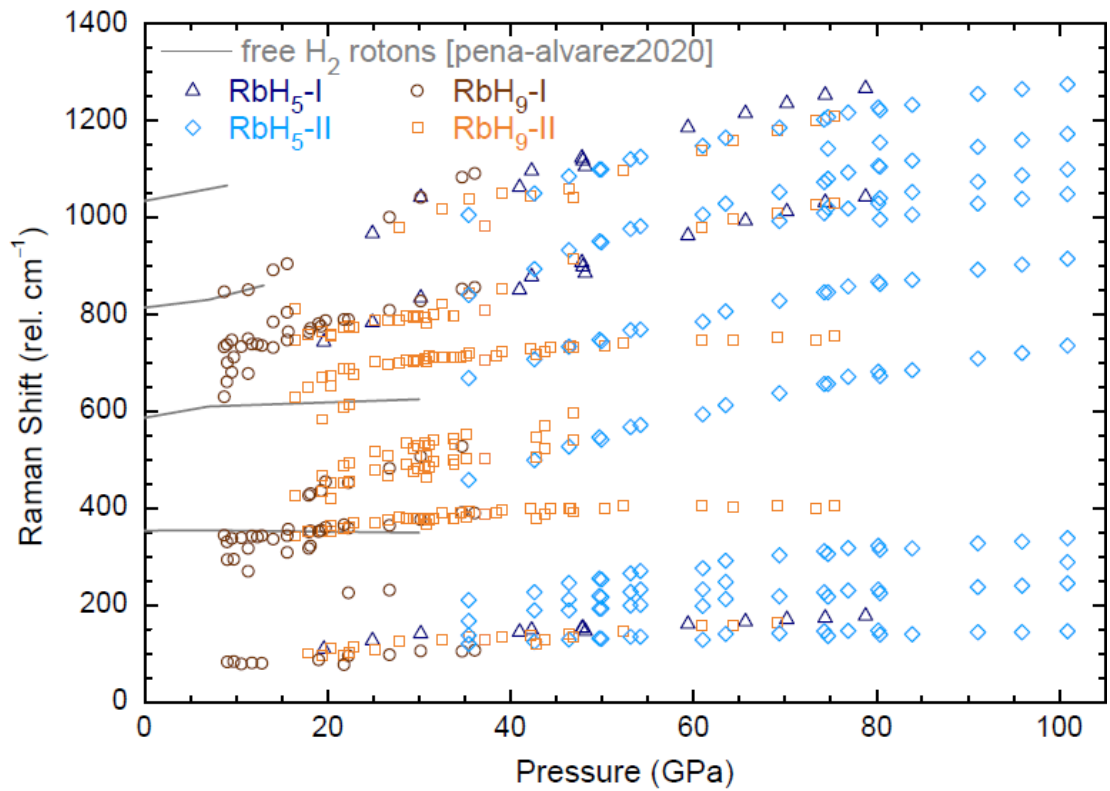


**Fig. SM3.** Frequency as a function of pressure of the low frequency Raman modes of the rubidium hydrides.

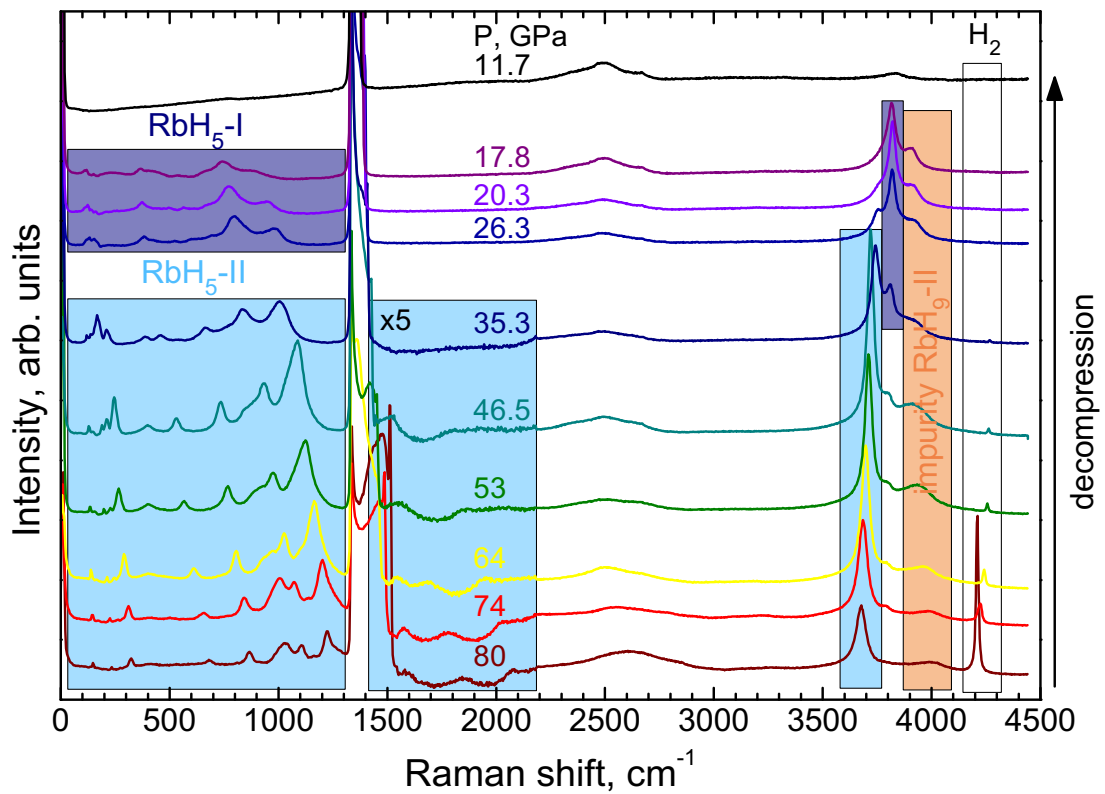


**Fig. SM4.** Characteristic Raman spectra of  $\text{RbH}_5\text{-II}$ , recorded in run 21 upon decompression at room temperature.

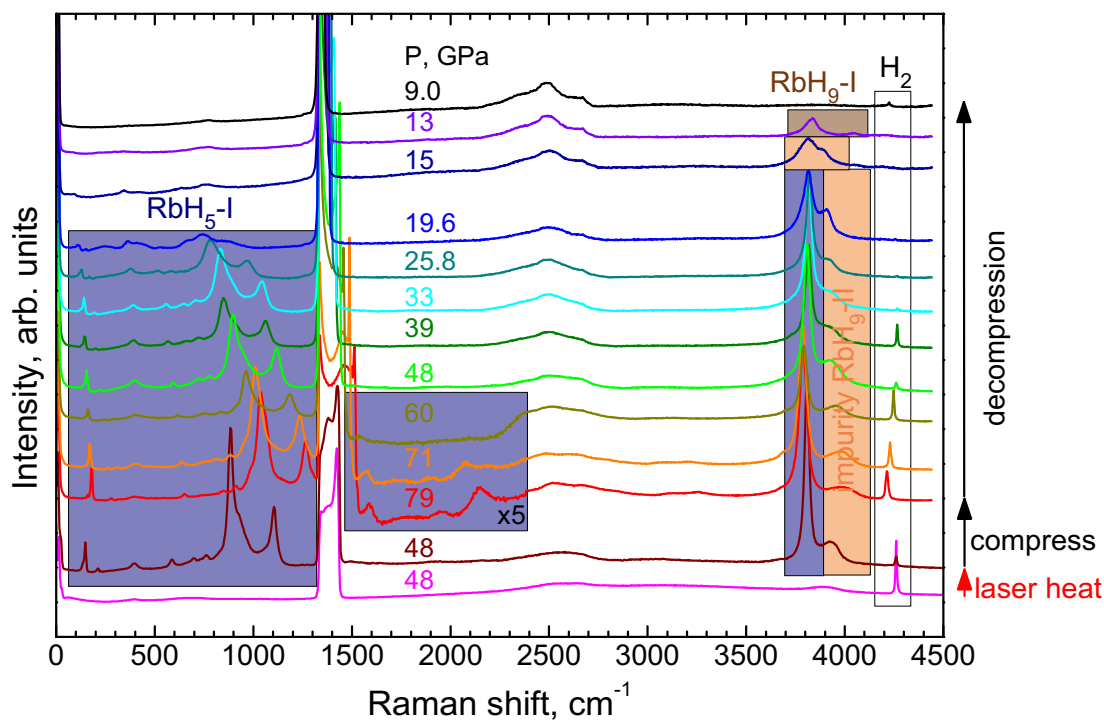


**Fig. SM5.** Characteristic Raman spectra of RbH<sub>5</sub>-I, recorded in run 21 upon laser heating, compression and decompression at room temperature.

### Impurities

Rubidium metal is extremely reactive with oxygen and moisture, and even in the glovebox with O<sub>2</sub> and H<sub>2</sub>O levels below 0.1 ppm it will oxidize within half an hour. The most common impurity, present in trace amounts in runs 1, 2, 6, 7, 9, 10, 13-19, and 21 is RbOH, which manifests itself in a Raman peak at 3300-3500 cm<sup>-1</sup>. We carefully checked all samples after gas loading for the presence of RbOH impurity, and discarded all samples where RbOH contamination was appreciable (around 20 loadings). Only clean samples were included in the present study. In some experiments (runs 6, 12, 14, 16, 18) we observed a formation of a new phase after laser heating at pressures between 24-56 GPa. This phase has a diamond-like structure of metal lattice (see Fig. SM6) with an extremely large atomic volume of ~92 Å<sup>3</sup> per metal atom at 30 GPa. The Raman spectrum of this phase comprise a sharp bound H<sub>2</sub> vibron at 4110 cm<sup>-1</sup> with weaker satellites at higher frequencies, and a sharp mode at 2280 cm<sup>-1</sup> with a lower frequency satellite mode (Fig. SM7). Upon decompression, this phase decomposed into RbH<sub>9</sub>-I at around 15 GPa (runs 6, 12, 14, 18). We must note that according to XRD the decomposition products of this phase in run 6 were heavily contaminated with rhenium hydride, and we cannot exclude if this phase is a ternary rhenium-rubidium-hydrogen compound, formed at the interface between the sample and the gasket. Despite all efforts, we were unable to synthesize this phase in runs 13, 20 and 21 despite extensive laser heating. Excessive laser heating can also promote a reaction between hydrogen and the diamond anvil (run 13), resulting in a formation of complex van der Waals compounds of hydrogen and methane, e.g. (CH<sub>4</sub>)<sub>3</sub>(H<sub>2</sub>)<sub>25</sub> [ranieri2022]. In contrast to rubidium superhydrides, these compounds demonstrate a bound H<sub>2</sub> vibron, which has a frequency higher than that of pure H<sub>2</sub>, and a sharp methane vibron at 3000-3100 cm<sup>-1</sup>.

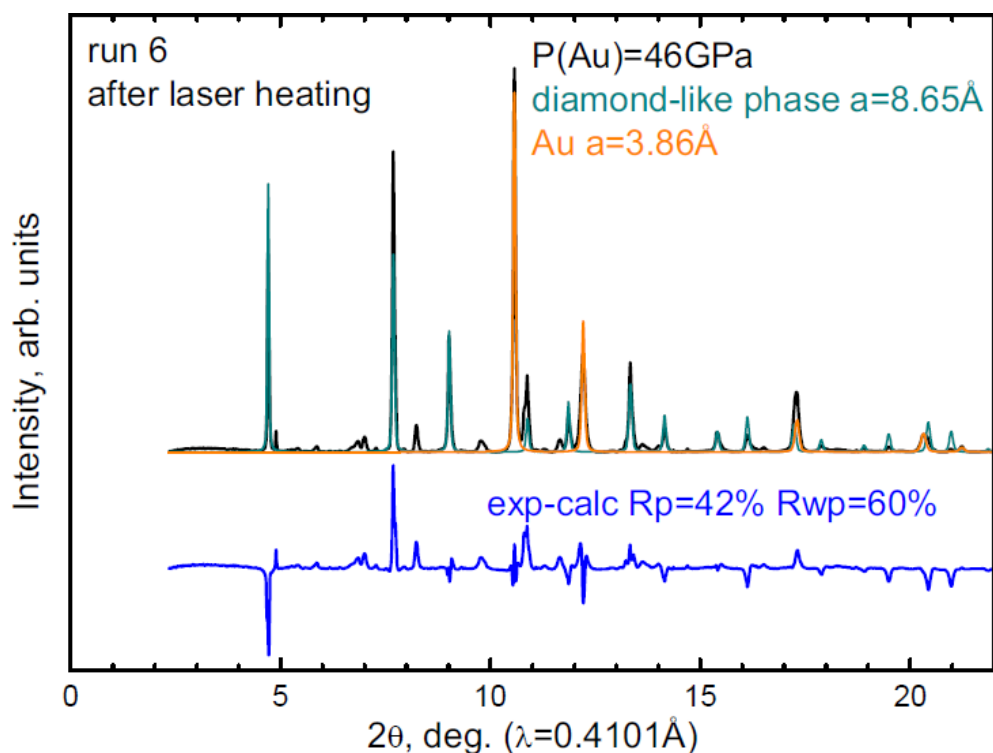


**Fig. SM6.** XRD pattern of diamond-like phase, collected in run 6 after laser heating at 46 GPa, and the results of the Rietveld refinement. The black curve is the experimental data, the cyan and orange curves show the calculated contributions from the diamond-like phase and gold, respectively, and the blue curve is Rietveld residual.

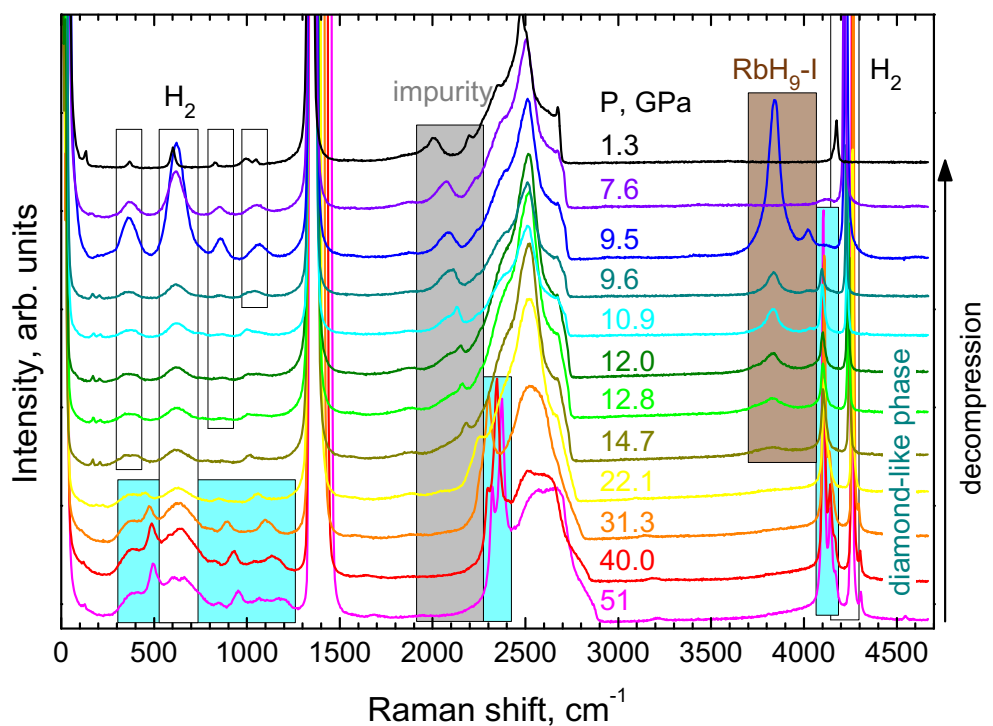


**Fig. SM7.** Characteristic Raman spectra of diamond-like phase, recorded in run 14 upon decompression at room temperature.

## Vegard's law

It was empirically found that in many systems, including hydrides [fukai2005] and superhydrides [guigue2020] the atomic volume is a linear function of composition. This empirical relation, called Vegard's law, can be used to justify hydrogen content of newly discovered superhydrides. We plotted the dependence of atomic volumes of all rubidium hydrides, extrapolated to 50 GPa, as a function of their composition, in Fig. SM8. The volumes of all phases follow a common linear trend. The hydrogen-induced volume expansion in rubidium hydrides at 50 GPa is close to the volume of pure hydrogen,  $\frac{1}{2}V(\text{H}_2) \approx 3.11 \text{ \AA}^3 / \text{H atom}$  [joubert2010] (dashed black line in Fig. SM8), which is considerably higher than the typical values of hydrogen-induced volume expansion in transition and rare-earth metal hydrides  $\frac{dV}{d(H/Me)} \approx 2.0 - 2.5 \text{ \AA}^3 / \text{H atom}$  [fukai2005, guigue2020]. The reason for that is that hydrogen in the crystal structure of transition and rare-earth metal hydrides is present in an atomic form, whereas in rubidium superhydrides it is mostly present in the form of  $\text{H}_2$  and  $\text{H}_3^-$  quasi-molecular units.

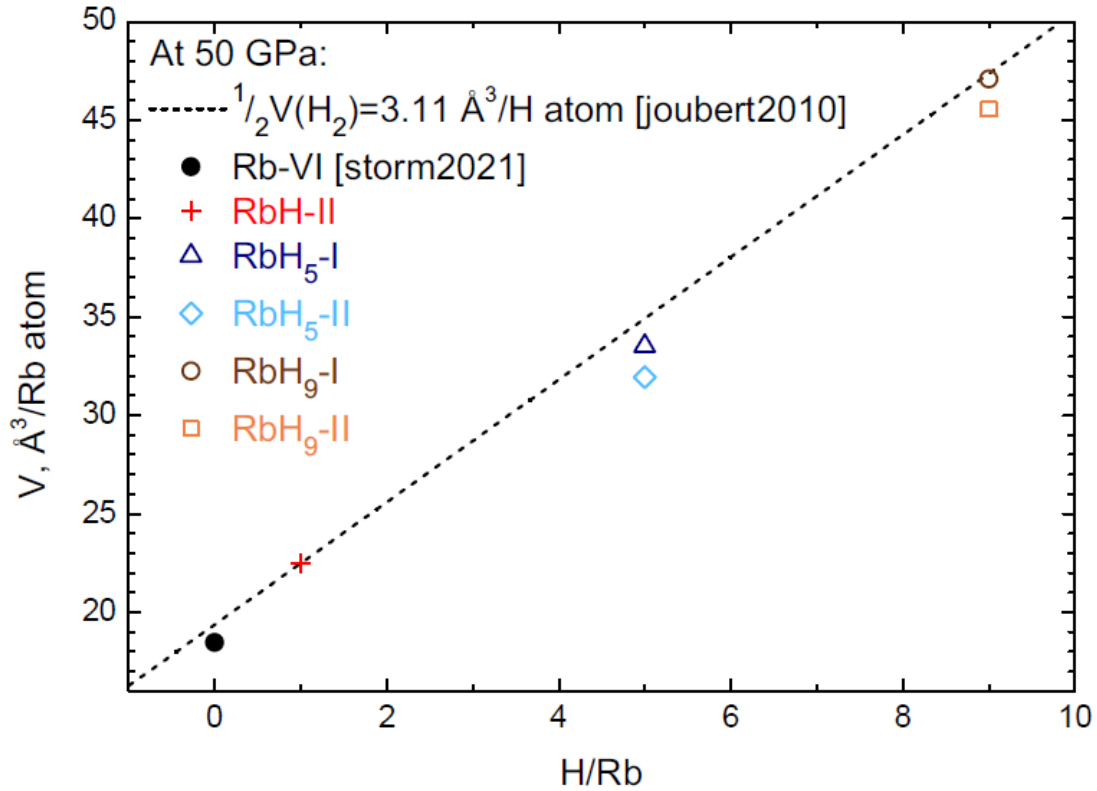


**Fig. SM8.** The dependence of the atomic volumes of rubidium [storm2021] and its hydrides, extrapolated to 50 GPa, on their H/Rb content. The slope of the dashed black line corresponds to the atomic volume of pure hydrogen at this pressure [joubert2010].

## Composition-pressure phase diagram of the Rb-H system at room temperature

There is a universally accepted opinion that the baric hysteresis for the formation reactions is highly asymmetric in the metal-hydrogen systems, and the equilibrium pressure is much closer to the decomposition pressure of a higher hydride, rather than to the midpoint between formation and decomposition pressures [antonov2004] because of the differences in microscopic mechanisms of hydride formation and decomposition. It is not entirely clear, however, if this rationale is applicable to congruent transformations, like  $\text{RbH}_9 - \text{I} \leftrightarrow \text{RbH}_9 - \text{II}$  and  $\text{RbH}_5 - \text{I} \leftrightarrow \text{RbH}_5 - \text{II}$ , disproportionation reactions, like  $\text{RbH}_5 - \text{I} \rightarrow \frac{1}{2}\text{RbH}_9 - \text{II} + \frac{1}{2}\text{RbH} - \text{II}$ , or in situations when higher hydride decomposes upon compression, like  $\text{RbH}_9 - \text{II} \rightarrow \text{RbH}_5 - \text{II} + 2\text{H}_2$ . In the tentative composition-pressure phase diagram of the Rb-H system, shown in Fig. SM9, we displayed these equilibria with dashed lines, and the rest of the equilibria with solid lines.

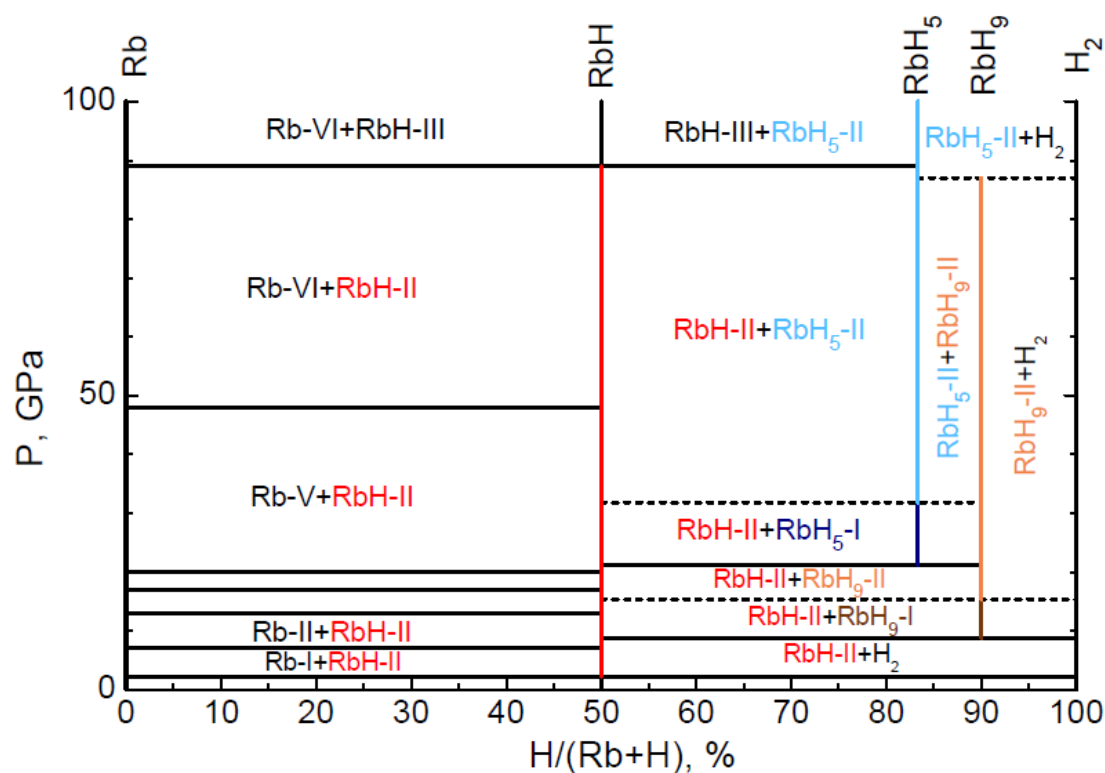


**Fig. SM9.** Composition-pressure phase diagram of the Rb-H system at room temperature.

## Crystal Structure Prediction

Crystal structure prediction (CSP) searches were carried out using the XTALOPT [lonie2011, falls2020] evolutionary algorithm release 12 [avery2019], which enables the prediction of stable and metastable structures starting from the composition alone. XTALOPT was interfaced with VASP (the Vienna ab initio Simulation Package) [kresse1996prb, kresse1996cms] for the density functional theory (DFT) structural relaxations (shape, volume, and atomic positions) performed using a three-step procedure. CSP searches were run to find the low-lying configurations for RbH<sub>5</sub> and RbH<sub>9</sub> at 10, 20, 50, and 100 GPa with up to 8 formula units in the primitive cell. An initial population of 80 random structures [avery2017, lonie2012] was created for the first generation. The likelihood that a particular structure was chosen for procreation was based on its 0 K enthalpy. The breeding operations and their relative probabilities were: (i) strippling (50%), (ii) permustrain (35%), and (iii) crossover (15%). The maximum number of generated structures in each search was set to 2000.

In order to identify the thermodynamically metastable Rb-H phases, we utilized a constrained evolutionary algorithm (EA) [Wang2023], which exclusively retains those structures in the parent pool that adhere to a given geometric criteria (here chosen to be *Imma* and *P6/mmm* symmetry of the Rb sublattice for RbH<sub>5</sub> at 100 GPa and RbH<sub>9</sub> at 20 GPa, respectively, according to the experimental XRD data), while disregarding those that do not meet these conditions. The constrained EA search was executed by using XTALOPT interfaced with Pymatgen [ong2013].

## Details of DFT Computations

Geometry optimizations and electronic structure calculations (electronic densities of states and band structures, electron localization functions (ELF) [Savin1997]) were performed using the projector augmented wave (PAW) method [blochl1994, kresse1999] implemented in VASP [kresse1996prb, kresse1996cms]. The exchange-correlation energy was treated within the Perdew-Burke-Ernzerhof (PBE) [perdew1996] generalized gradient approximation (GGA). The evolutionary searches used an energy cutoff of 800 eV for the plane-wave basis and a  $\Gamma$ -centered Monkhorst-Pack scheme [monkhorst1976], where the number of divisions along each reciprocal-lattice vector was chosen such that its product with the real lattice constant was 30 Å. These values were increased to 1000 eV and 50 Å for precise re-optimizations and electronic structure calculations. All structures were optimized until the net forces on atoms were below 1 meV/Å, and the difference in enthalpy between two self-consistent steps was less than 1 meV/atom. The LOBSTER package [Maintz2016] was used to calculate the crystal overlap Hamilton populations (COHPs) for the bonding analysis, and Mulliken atomic charges [Mulliken1955, Ertural2019]. Test calculations showed that equations of states computed with the PBE, PBEsol and DFT-D3 functionals for the two RbH<sub>9</sub> and RbH<sub>5</sub> phases were in consistent agreement with experimental observations.

In this work, first-principles phonon calculations using the finite displacements method at the quasi-harmonic level were performed using the open-source package PHONOPY (<https://phonopy.github.io/phonopy/>). Supercell structures with or without displacements are created from a reference unit cell considering all possible crystal

symmetry operations. In general, a 2 x 2 x 2 supercell is sufficient, but larger ones can be required to avoid unphysical imaginary frequencies. Force constants are calculated using the optimized structure using VASP.

### Predicted structural parameters

**Table SMIV.** Structural parameters of Rb-H phases at the PBE level of theory.

Phase	Pressure (GPa)	Space group	Z	Lattice parameters (Å)	Atomic coordinates (fractional)
RbH	20	<i>Pm-3m</i>	1	$a=b=c=3.058$	Rb 0.000 0.000 0.000 H 0.500 0.500 0.500
RbH	100	<i>Cmcm</i>	4	$a=2.830,$ $b=7.881,$ $c=3.174$	Rb 0.000 0.139 0.750 H 0.000 0.426 0.750
RbH <sub>5</sub>	20	<i>Cmcm</i>	4	$a=3.519,$ $b=8.398,$ $c=5.630$	Rb 0.000 0.416 0.750 H 0.000 0.127 0.576 H 0.000 0.284 0.181 H 0.000 0.124 0.750
RbH <sub>5</sub>	50	<i>Pnn2</i>	4	$a=5.401,$ $b=5.567,$ $c=4.362$	Rb 0.000 0.000 0.358 Rb 0.000 0.500 0.104 H 0.090 0.639 0.625 H 0.127 0.170 0.826 H 0.167 0.859 0.903 H 0.213 0.655 0.514 H 0.227 0.330 0.519
RbH <sub>9</sub>	20	<i>Cmc2<sub>1</sub></i>	4	$a=4.598,$ $b=7.090,$ $c=7.378$	Rb 0.000 0.313 0.264 H 0.196 0.038 0.521 H 0.202 0.422 0.948 H 0.000 0.031 0.700 H 0.000 0.131 0.860 H 0.000 0.202 0.943 H 0.000 0.246 0.642 H 0.000 0.354 0.626
RbH <sub>9</sub>	20	<i>Cccm</i>	4	$a=4.303,$ $b=7.599,$ $c=7.094$	Rb 0.000 0.000 0.250 H 0.036 0.322 0.299 H 0.046 0.457 0.500 H 0.161 0.753 0.500 H 0.250 0.250 0.500
H <sub>2</sub> <sup>a</sup>	100	<i>P6<sub>3</sub>/m</i>	8	$a=b=3.765,$ $c=2.997$	H 0.067 0.266 0.250 H 0.098 0.708 0.250 H 0.333 0.667 0.628

<sup>a</sup> Structure taken from [pickard2007]

**Table SMV.** Calculated enthalpies ( $H$ ) and zero-point energy (ZPE) of the predicted RbH<sub>5</sub> and RbH<sub>9</sub> compounds at different pressures. The most stable phase is highlighted in black.

Phase	Pressure (GPa)	Space group	$H$ (eV/atom)	ZPE (eV/atom)	$\Delta H + \Delta ZPE$ (eV/atom)
RbH <sub>5</sub>	30	<b><i>Cmcm</i></b> <b>(RbH<sub>5</sub>-I)</b>	-1.450	0.195	0.000
		<i>Pnn2</i> (RbH <sub>5</sub> -II)	-1.417	0.192	+0.030
	100	<b><i>Cmcm</i></b>	0.818	0.240	0.000
		<i>Pnn2</i>	0.836	0.232	+0.010
RbH <sub>9</sub>	10	<i>Cmc2<sub>1</sub></i> (RbH <sub>9</sub> -I)	-2.593	0.189	+0.017
		<i>Cccm</i> (RbH <sub>9</sub> -II)	-2.606	0.190	+0.005
		<b><i>Cm</i><sup>a</sup></b>	-2.611	0.190	0.000
	20	<i>Cmc2<sub>1</sub></i>	-2.190	0.200	+0.020
		<b><i>Cccm</i></b>	-2.214	0.204	0.000
		<i>Cm</i> <sup>a</sup>	-2.207	0.203	+0.006
	50	<i>Cmc2<sub>1</sub></i>	-1.235	0.222	+0.025
		<b><i>Cccm</i></b>	-1.268	0.230	0.000
		<i>Cm</i> <sup>a</sup>	-1.237	0.228	+0.029
		<i>P6<sub>3</sub>/mmc</i>	-1.261	0.229	+0.006
	100	<i>Cmc2<sub>1</sub></i>	0.032	0.251	+0.055
		<i>Cccm</i>	-0.023	0.254	+0.003
<b><i>P6<sub>3</sub>/mmc</i></b>		-0.027	0.255	0.000	

<sup>a</sup> Structures taken from [zhou2024]

## Dynamical stability

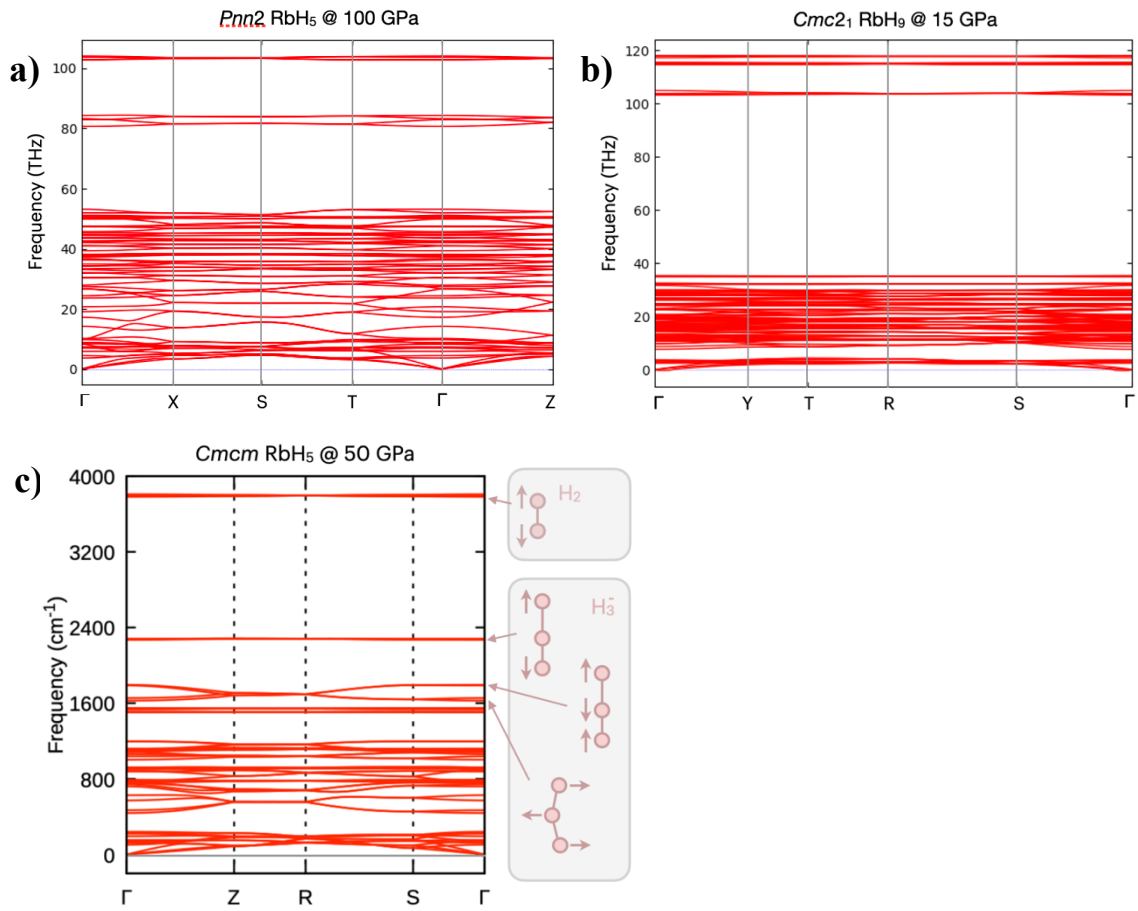


**Fig. SM10.** Phonon dispersion curves of (a) *Pnn2* RbH<sub>5</sub>-II at 100 GPa, (b) *Cmc2<sub>1</sub>* RbH<sub>9</sub>-I at 15 GPa, and (c) *Cmcm* RbH<sub>5</sub>-I at 50 GPa. No imaginary phonon modes are found in the whole Brillouin zone. This confirms the dynamical stability of each phase. The high-frequency bands associated with stretching modes of H<sub>3</sub><sup>-</sup> and H<sub>2</sub> in *Cmcm* RbH<sub>5</sub>-I are shown in (c). The inset illustrates the motions of the atoms within the H<sub>3</sub><sup>-</sup> units associated with a particular frequency.

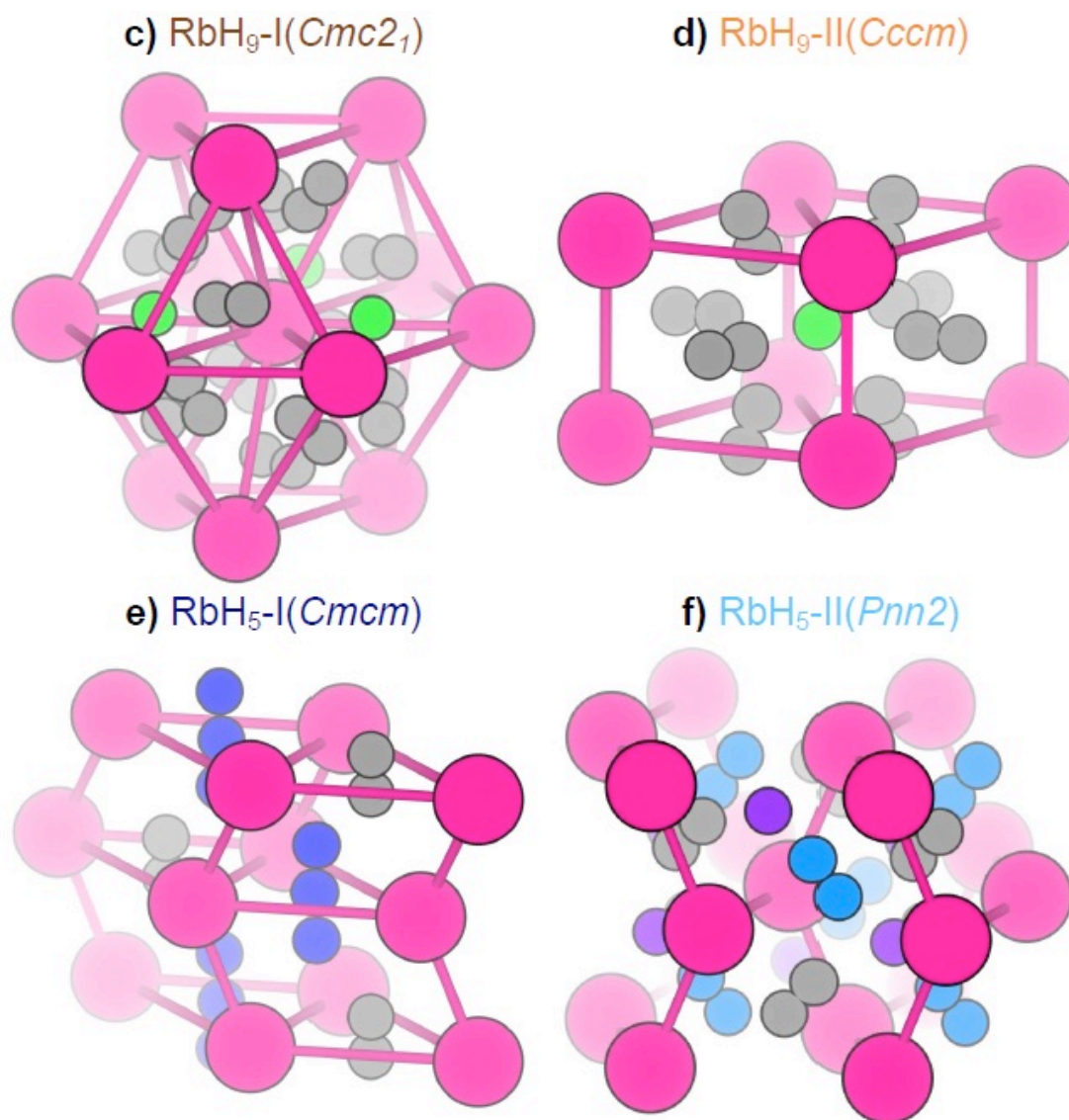


**Figure SM11.** Predicted structural models of rubidium superhydrides (see Table SMIV for crystal structure parameters). Rubidium atoms are pink, quasi-molecular  $\text{H}_2$  units are grey, and  $\text{H}^-$  are green. For  $\text{RbH}_5\text{-I}(\text{Cmcm})$ , the linear  $\text{H}_3^-$  anions are represented by dark blue atoms. For  $\text{RbH}_5\text{-II}(\text{Pnn}2)$ , the asymmetric  $\text{H}_3^-$  anions comprise  $\text{H}_2$  units (light blue) and nearest neighbour  $\text{H}^-$  (purple).

**Table SMVI.** The negative of the integrated crystal orbital Hamilton population (-ICOHP) of the hydrogen motifs. The bond types are associated with the hydrogen atoms depicted in Fig. 2c-f

Phase	Bond type	Distance (Å)	-ICOHP (eV/bond)
<i>Cmcm</i> RbH <sub>5</sub> at 50 GPa	H1 - H1'	0.790	4.84
	H2-H3	0.950	3.21
<i>Pnn2</i> RbH <sub>5</sub> at 50 GPa	H1 - H2	0.805	4.70
	H3 - H4	0.867	4.11
	H4 - H5	1.128	1.98
<i>Cccm</i> RbH <sub>9</sub> at 50 GPa	H1 - H1'	0.777	5.36
	H2-H2'	0.775	5.47
	H1-H3	1.619	0.29
<i>Cmc2<sub>1</sub></i> RbH <sub>9</sub> at 20 GPa	H1 - H2	0.767	5.60
	H3 - H4	0.804	4.71
	H1 - H5	1.585	0.37

### Calculated Raman spectra

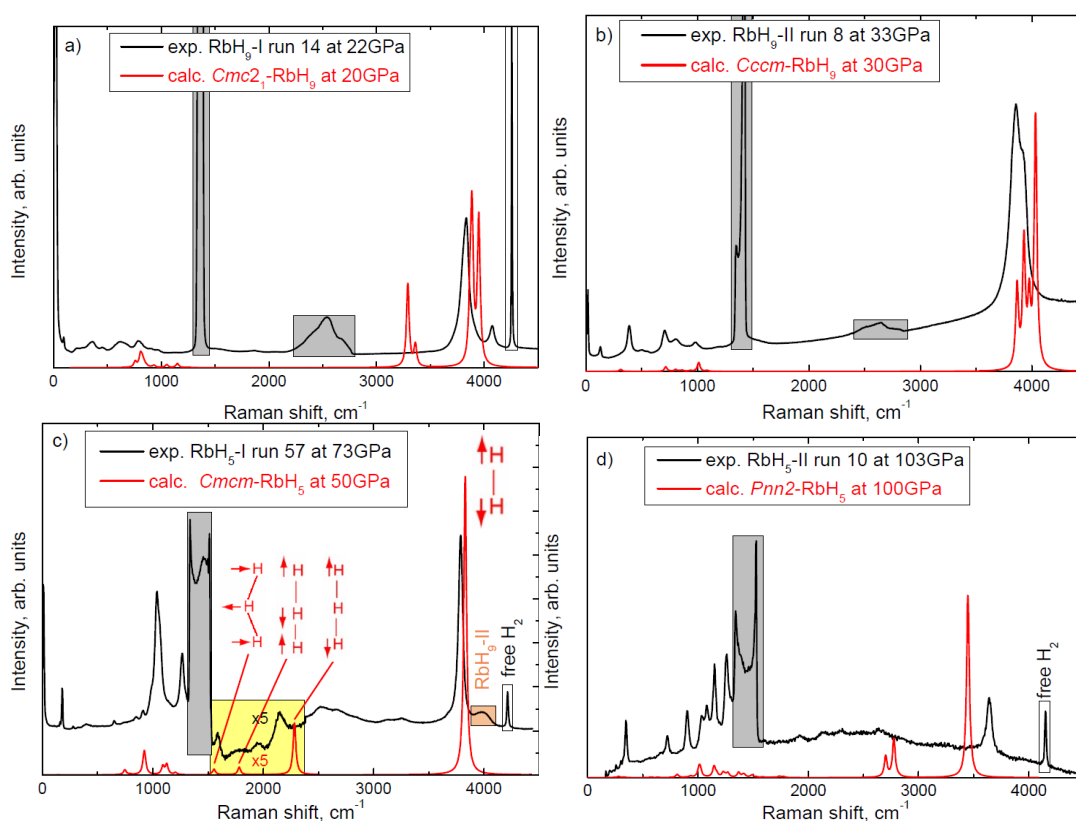


**Fig. SM12.** The calculated (red) and observed (black) Raman spectra of (a) *Cmc2<sub>1</sub>* RbH<sub>9</sub>, (b) *Cccm* RbH<sub>9</sub>, (c) *Cmcm* RbH<sub>5</sub> and (d) *Pnn2* RbH<sub>5</sub> at selected pressures. Peaks from the diamond anvils are highlighted in grey, the free H<sub>2</sub> vibron is indicated with a black rectangle and in (c) RbH<sub>9</sub>-II is highlighted in orange.

We calculated the Raman spectra of the  $Cmc2_1$  and  $Cccm$   $RbH_9$  crystal structures at 20 and 30 GPa, as well as of the  $Cmcm$  and  $Pnn2$  phases of  $RbH_5$  at pressures of 50 and 100 GPa. The results were subsequently compared with the obtained experimental results (see Fig. SM12). Our calculations underestimated the position of the spectral peak at  $\sim 3625\text{ cm}^{-1}$  for  $Pnn2$ - $RbH_5$  at 103 GPa. It should be noted that quantum nuclear and anharmonic effects, not considered here, may be key in renormalizing the frequencies and line shapes of these modes, as has been shown in the case of pure hydrogen [monacelli2021].

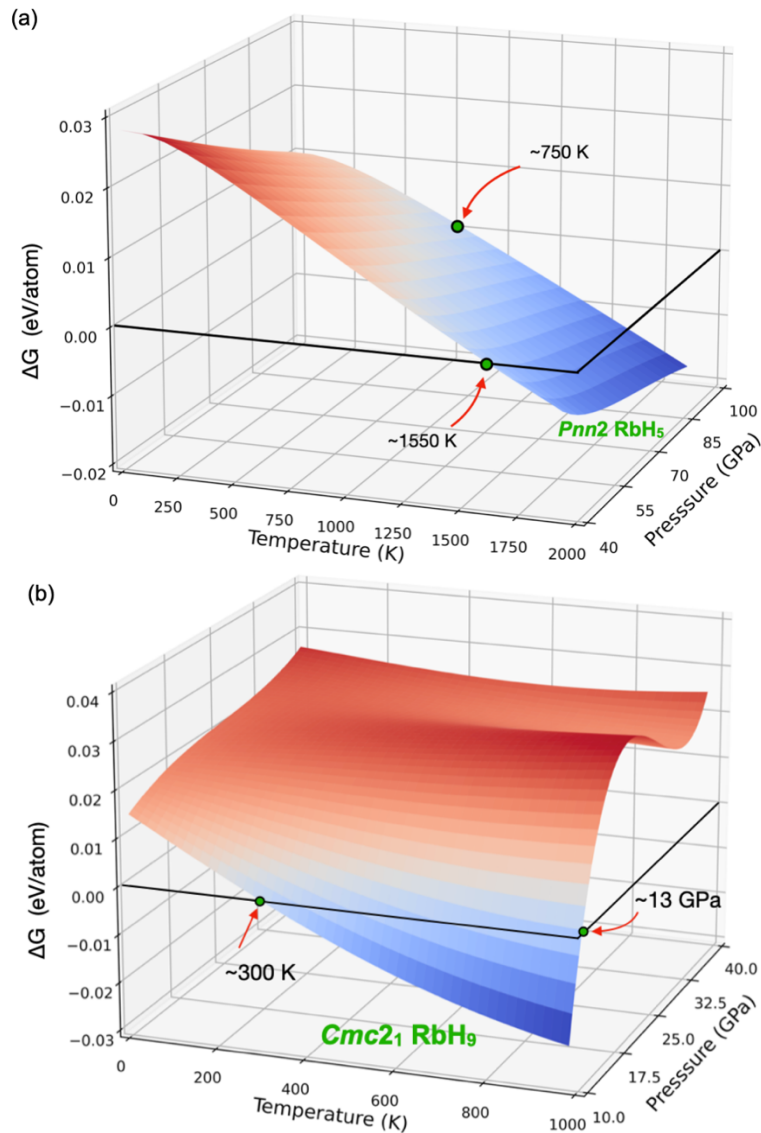


**Fig. SM13.** The calculated Gibbs Free energies of (a)  $Pnn2$  relative to  $Cmcm$   $RbH_5$  and (b)  $Cmc2_1$  relative to  $Cccm$   $RbH_9$  as a function of temperature,  $T$ , and pressure,  $P$ . A negative  $\Delta G$  (blue region) indicates conditions where  $Pnn2$   $RbH_5$  and  $Cmc2_1$   $RbH_9$  are more stable than  $Cmcm$   $RbH_5$  and  $Cccm$   $RbH_9$ , respectively. The green dots with red arrows highlight the equilibrium conditions where  $Pnn2$   $RbH_5$  and  $Cmc2_1$   $RbH_9$  become preferred.

The temperature has an impact on the relative stabilities of  $Pnn2$   $RbH_5$  and  $Cmc2_1$   $RbH_9$ , which were predicted by the constrained evolutionary algorithm search.  $Pnn2$   $RbH_5$  has an energy that is 18 meV/atom higher than the ground state stable phase  $Cmcm$  at 100 GPa and 0 K (with +10 meV/atom accounted for the ZPE effect), and it is less stable by 33 meV/atom at 30 GPa and 0 K (with +30 meV per atom accounted for the ZPE effect) (See Table SM V). The calculation of Gibbs free energy suggests that at temperatures above  $\sim 750$  K and under 100 GPa, the  $Pnn2$   $RbH_5$  phase is more stable than the  $Cmcm$  phase. However, with decompression, a higher temperature is required to stabilize the  $Pnn2$  phase compared to the  $Cmcm$  phase. For example, at pressures below 40 GPa, the  $Pnn2$  phase is only more stable above 1550 K, see Fig. SM13 (a). The  $Cmc2_1$   $RbH_9$  exhibits an energy of 12 meV/atom higher than the  $Cccm$  structure at 10 GPa (with ZPE effect). However, the calculation of Gibbs free energy shows that at  $Cmc2_1$   $RbH_9$  turns out to be more stable rather than  $Cccm$  at 13 GPa and above the room-temperature (300 K), see Fig. SM13 (b).

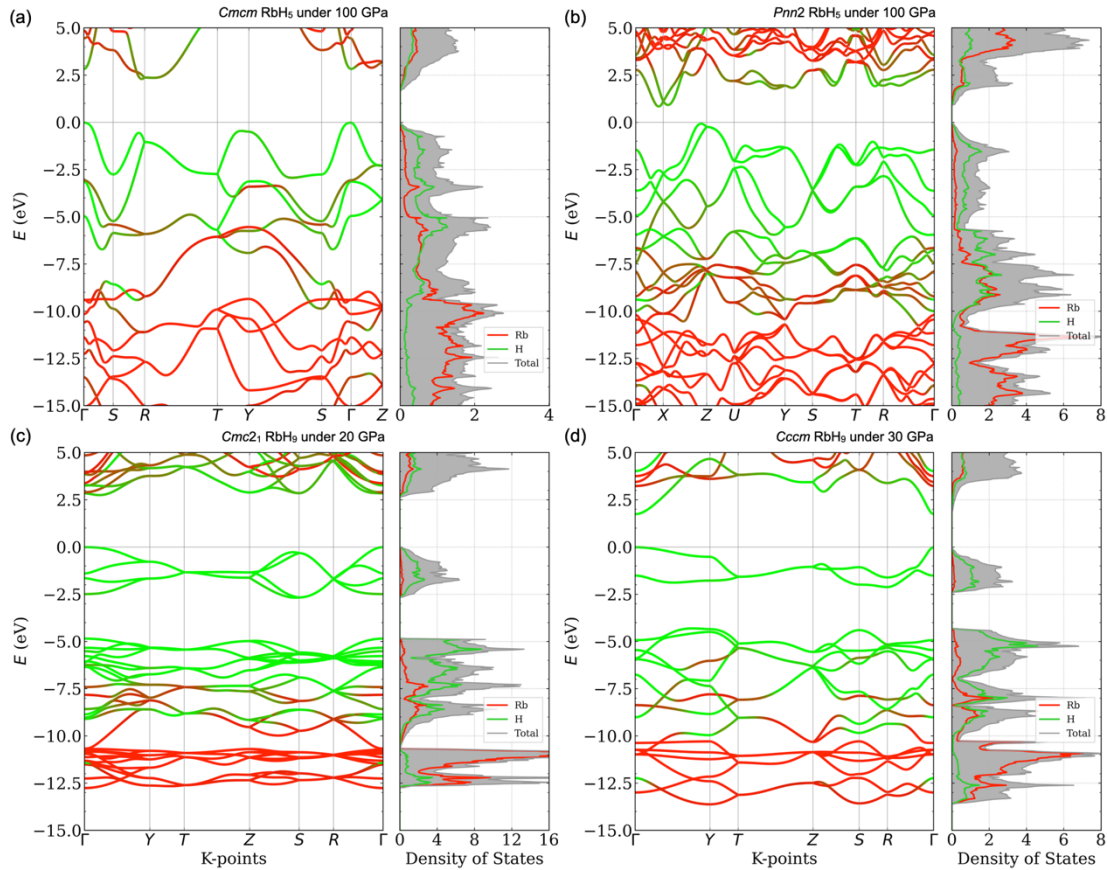


**Fig. SM14.** The calculated band structure and density of states for (a)  $Cmcm$  and (b)  $Pnn2$   $RbH_5$ , (c)  $Cmc2_1$  and (d)  $Cccm$   $RbH_9$  under pressure. The presence of a band gap indicates that the  $RbH_5$  and  $RbH_9$  phases exhibit insulating properties.

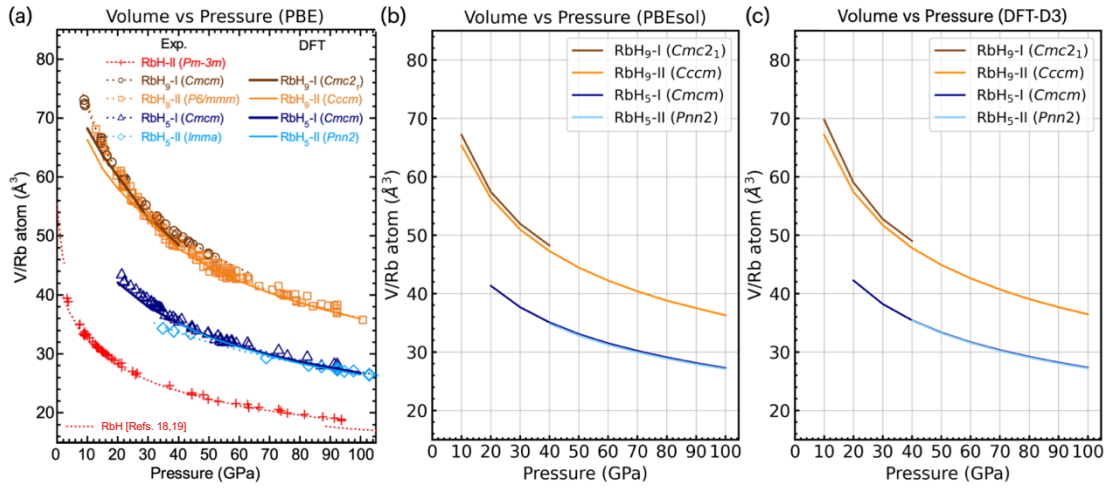


**Fig. SM15** Volume as a function of pressure for the observed rubidium hydrides by using (a) PBE, (b) PBEsol, (c) DFT-D3 functionals.

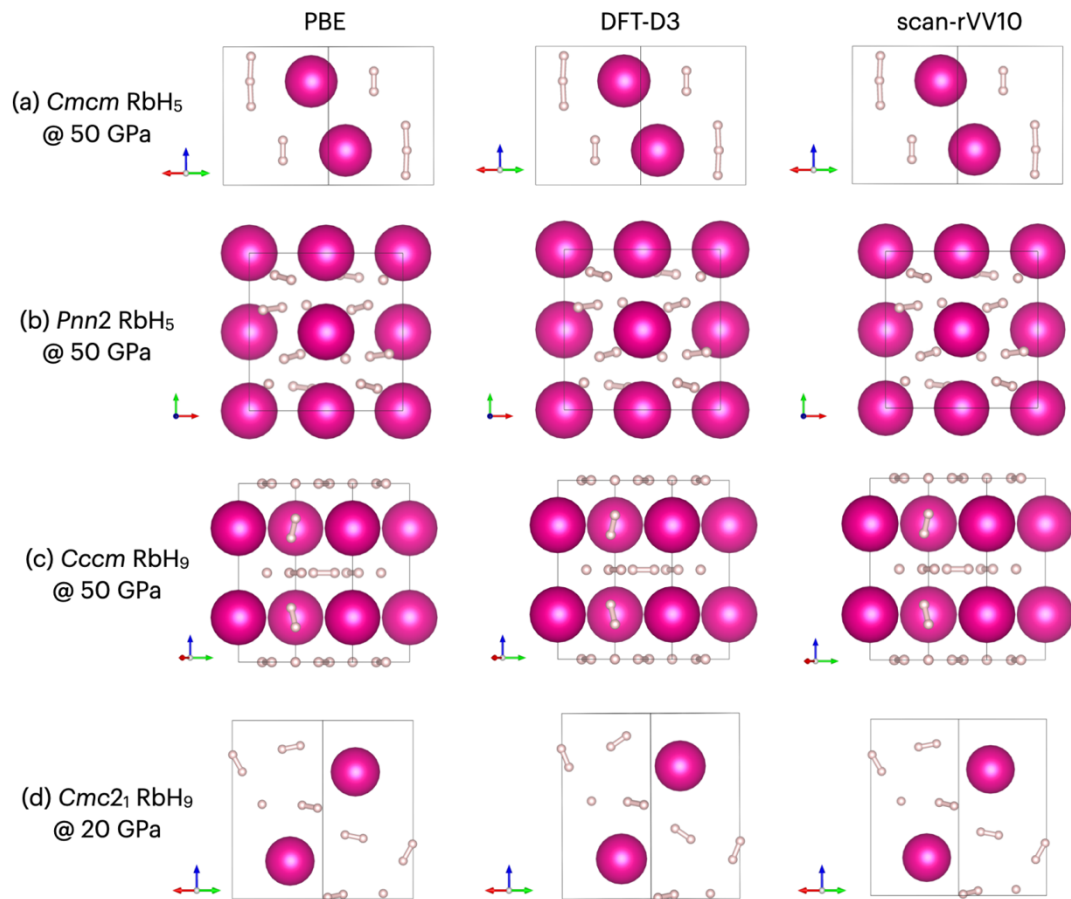


**Fig. SM16** The geometry optimized crystal structure of (a)  $Cmc2_1$   $RbH_9$  at 20 GPa, (b)  $Pnn2$   $RbH_5$  at 50 GPa, (c)  $Cccm$   $RbH_9$  at 50 GPa, and (d)  $Cmc2_1$   $RbH_9$  at 20 GPa by using PBE, DFT-D3, and scan-rVV10 functionals, respectively.

## References

- [liermann2015] H.-P. Liermann et al, *J. Synchrotron Radiat.* **22**, 908–924 (2015).
- [merlini2013] M. Merlini et al, *High Pressure Res.* **33**, 511–522 (2013).
- [prakapenka2008] V. B. Prakapenka et al, *High Pressure Res.* **28**, 225-235 (2008).
- [anzellini2018] S. Anzellini et al, *J. Synchrotron Radiat.* **25**, 1860-1868 (2018).
- [prescher2015] C. Prescher et al, *High Pressure Res.* **35**, 223-230 (2015).
- [kraus1996] W. Kraus et al, *J. Appl. Cryst.* **29**, 301–303 (1996).
- [dorfman2012] S. M. Dorfman et al, *J. Geophys. Res.* **117**, B08210 (2012).
- [ghandehari1995] K. Ghandehari et al, *Mod. Phys. Lett. B* **9**, 1133-1140 (1995).
- [howie2012] R. T. Howie et al, *Phys. Rev. Lett.* **108**, 125501 (2012).
- [akahama2006] Y. Akahama et al, *J. Appl. Phys.* **100**, 043516 (2006).
- [mao1986] H. K. Mao et al, *J. Geophys. Res.* **91**, 4673-4676 (1986).
- [birch1947] F. Birch, *Phys. Rev.* **71**, 809–824 (1947).
- [pena-alvarez2020] M. Pena-Alvarez et al, *J. Phys. Chem. Lett.* **11**, 6626–6631 (2020).
- [ranieri2022] U. Ranieri et al, *Phys. Rev. Lett.* **128**, 215702 (2022).
- [fukai2005] Y. Fukai, *The Metal-Hydrogen System*, 2nd ed.; Springer-Verlag: Berlin-Heidelberg, 104-113 (2005).
- [guigue2020] B. Guigue et al, *Phys. Rev. B* **102**, 014107 (2020).
- [joubert2010] J.-M. Joubert, *Int. J. Hydrogen Energy* **35**, 2104–2111 (2010).
- [storm2021] C. V. Storm et al, *Phys. Rev. B* **103**, 224103 (2021).
- [antonov2004] V. E. Antonov et al, *J. Phys.: Condens. Matter* **16**, 8387–8398 (2004).
- [lonie2011] D. C. Lonie & E. Zurek, *Comput. Phys. Commun.* **182**, 372–387 (2011).
- [falls2020] Z. Falls et al., *J. Phys. Chem. C* **125**, 1601–1620 (2020).
- [avery2019] P. Avery et al., *Comput. Phys. Commun.* **237**, 274–275 (2019).
- [kresse1996prb] G. Kresse & J. Furthmuller, *Phys. Rev. B* **54**, 11169 (1996).
- [kresse1996cms] G. Kresse & J. Furthmuller, *J. Comput. Mater. Sci.* **6**, 15–50 (1996).
- [avery2017] P. Avery & E. Zurek, *Comput. Phys. Commun.* **213**, 208–216 (2017).
- [lonie2012] D. C. Lonie & E. Zurek, *Comput. Phys. Commun.* **183**, 690–697 (2012).
- [Wang2023] B. Wang et al. *J. Chem. Theory Comput.* **19**, 7960–7971 (2023).
- [ong2013] S. P. Ong et al., *Comp. Mat. Sci.* **68**, 314-319 (2013).
- [Savin1997] A. Savin et al., *Angew. Chem. Int. Ed.* **36**, 1808–1832 (1997).
- [blochl1994] P. E. Blochl, *Phys. Rev. B* **50**, 17953 (1994).
- [kresse1999] G. Kresse & D. Joubert, *Phys. Rev. B* **59**, 1758 (1999).
- [perdew1996] J. P. Perdew et al., *Phys. Rev. Lett.* **77**, 3865 (1996).
- [monkhorst1976] H. Monkhorst & J. D. Pack, *Phys. Rev. B* **13**, 5188 (1976).
- [Maintz2016] S. Maintz et al., *J. Comput. Chem.* **37**, 1030–1035 (2016).
- [Mulliken1955] R. S. Mulliken, *J. Chem. Phys.* **23**, 1833-1840 (1955).
- [Ertural2019] C. Ertural et al., *RSC Adv* **9**, 29821 (2019).
- [pickard2007] C. J. Pickard, R. J. Needs, *Nature Phys.* **3**, 473–476 (2007).
- [zhou2024] D. Zhou et al., *Adv. Energy Mater.* **14**, 2400077 (2024).
- [monacelli2021] L. Monacelli et al., *Nature Phys.* **17**, 63-67 (2021).